A Regional multi-Air Pollutant Assimilation System (RAPAS v1.0) for emission estimates: system development and application

Shuzhuang Feng[1], Fei Jiang[1,2], Zheng Wu[3], Hengmao Wang[1,2], Wei He[1], Yang Shen[1], Lingyu Zhang[1], Yanhua Zheng[1], Chenxi Lou[1], Ziqiang Jiang[4], Weimin Ju[1,2]

[1] *Jiangsu Provincial Key Laboratory of Geographic Information Science and Technology, International Institute for Earth System Science, Nanjing University, Nanjing, 210023, China*

[2] *Jiangsu Center for Collaborative Innovation in Geographical Information Resource Development and Application, Nanjing, 210023, China*

[3] *Chongqing Institute of Meteorological Sciences, Chongqing, 401147, China*

[4] *Jiangsu Environmental Monitoring Center, Nanjing, 210019, China*

Correspondence to: Fei Jiang (jiangf@nju.edu.cn)

Abstract

Top-down atmospheric inversion infers surface-atmosphere fluxes from spatially distributed observations of atmospheric compositions, which is a vital means for quantifying large-scale anthropogenic and natural emissions. In this study, we developed a Regional multi-Air Pollutant Assimilation System (RAPAS v1.0) based on the Weather Research and Forecasting/Community Multiscale Air Quality Modeling System (WRF/CMAQ) model, the three-dimensional variational (3DVAR) algorithm and the ensemble square root filter (EnSRF) algorithm. It is capable of simultaneously assimilating spatially distributed hourly in-situ measurements of CO, SO_2, NO_2, $PM_{2.5}$ and PM_{10} concentrations to quantitatively optimize gridded emissions of CO, SO_2, NO_x, primary $PM_{2.5}$ ($PPM_{2.5}$) and coarse PM_{10} (PMC) on regional scale. RAPAS includes two subsystems, initial field assimilation (IA) subsystem and emission inversion (EI) subsystem, which are used to generate a good chemical initial condition (IC), and conduct inversions of anthropogenic emissions, respectively. A "two-step" inversion scheme is adopted in the EI subsystem in each data assimilation (DA) window, in which the emission is inferred in the first step, and then, it is input into the CMAQ model to simulate the initial field of the next window, meanwhile, it is also transferred to the next window as the prior emission. The chemical IC is optimized through the IA subsystem, and the original emission inventory is only used in the first DA window. Besides, a "super-observation" approach is implemented based on optimal estimation theory to decrease the computational costs and observation error correlations and reduce the influence of representativeness errors.

With this system, we estimated the emissions of CO, SO_2, NO_x, $PPM_{2.5}$ and PMC in December and July 2016 over China using the corresponding nationwide surface observations. The 2016 Multi-resolution Emission Inventory for China (MEIC 2016) was used as the prior emission. For December, the system was run from 26 November to 31 December, in which the IA subsystem was run in the first 5 days, and the EI subsystem was run in the following days. In July, the system was run in the same way. The evaluation and sensitivity testing of this system mainly focused on December.

Results showed that the simulated concentrations of CO, NO2, SO2, PM2.5 and PM10 with the prior inventory have large systematic biases, with relative biases in the range of -48.2-54.2%. In the IA subsystem, after 3DVAR, the root mean squared error (RMSE) of the simulated concentrations decreased by 50.0-73.2%, and the correlation coefficient (CORR) increased to 0.78-0.92 for the five species. In the EI subsystem, after emission inversions, the RMSE of the simulated concentrations decreased by 40.1-56.3%, and the CORR increased to 0.69-0.87. For the whole mainland China, the uncertainties were reduced by 44.4%, 45.0%, 34.3%, 51.8% and 56.1% for CO, SO_2, NO_x, $PPM_{2.5}$ and PMC, respectively. Overall, compared to the prior emission (MEIC 2016), the posterior emissions increased by 129%, 20%, 5%, and 95% for CO, SO_2, NO_x and $PPM_{2.5}$, respectively, indicating that there was significant underestimation in the MEIC inventory. The posterior PMC emissions, including anthropogenic and natural dust contributions, increased by 1045%. A series of sensitivity tests were conducted with different inversion processes, prior emissions, prior uncertainties, and observation errors. Results showed that the "two-step" scheme clearly outperformed the simultaneous assimilation of ICs and emissions ("one-step" scheme), and the system is rather robust in estimating the emissions using the nationwide surface observations over China. Our study offers a useful tool for accurately quantifying multi-species anthropogenic emissions at large scales and near-real time.

1. Introduction

Due to rapid economic developments and pollution control legislations, an increasing demand to provide updated emission estimates has arisen, especially in areas where anthropogenic emissions are intensive. Accurately estimating source emission quantities and spatiotemporal changes resulting from various regulations is imperative and valuable for understanding air quality responses and crucial for providing timely instructions for the design of future emissions regulations. However, most inventories have been developed based on a bottom-up approach and are usually updated with a few years delay due to the complexity of gathering all statistical information on activity levels and sector-specific emission factors (Ding et al., 2015). The large uncertainty associated with the low temporal and spatial resolution of these datasets also greatly limits the assessment of emission changes. Some studies (Bauwens et al., 2020; Shi and Brasseur, 2020) have evaluated emission changes indirectly through concentration measurements, but air pollution changes are not only dominated by emission changes, but also highly affected by meteorological conditions (Shen et al., 2021).

Top-down atmospheric inversion infers surface-atmosphere fluxes from spatially distributed observations of atmospheric compositions. Recent efforts have focused on developing air pollution data assimilation (DA) system to conduct the top-down inversion, which is able to integrate model and multi-source and large amounts of observational information to constrain emission sources. Two major methods, namely, 4D-variational data assimilation (4DVAR) and ensemble Kalman filter (EnKF), are widely used in those DA systems. 4DVAR provides a global optimal analysis through minimizing a cost function. It shows implicit flow-dependent background error covariance and can reflect complex nonlinear constraint relationship (Lorenc, 2003). Additionally, the model error can be partly accounted for with a weak constraint 4DVAR method through the definition of a systematic error term in a cost function (Derber, 1989). For example, GEOS-Chem and TM5 4DVAR frameworks have been used to estimate CH_4 (Alexe et al., 2015; Schneising et al., 2009; Stanevich et al., 2021; Wecht et al., 2014) and CO_2 fluxes (Basu et al., 2013; Nassar et al., 2011; Wang et al.,

2019a) from different satellite retrieval products. Monteil et al. (2013) showed that the global patterns of CH_4 emissions derived from SCIAMACHY (with bias correction) and GOSAT retrievals are in remarkable agreement based on 15 months observations. Additionally, Jiang et al. (2017) used 4DVAR algorithm to estimate global CO emission trends from 2000–2015 using MOPITT retrievals. Kurokawa et al. (2009) and Stavrakou et al. (2008) also used 4DVAR technique to estimate NO_x emission changes. However, the drawback of the 4DVAR method is the additional development of adjoint models that are technically difficult and cumbersome for complex chemical transport models. Instead, EnKF uses the flow-dependent background error covariance generated by ensemble simulations to map the deviations in concentrations to increments of emissions, which is more flexible and easier to implement. Many previous studies have used EnKF techniques to assimilate the single or dual species observations to optmize the corresponding emission species (Chen et al., 2019; Peng et al., 2017; Schwartz et al., 2014; Sekiyama et al., 2010). Multispecies data assimilation has shown the advantage of efficiently reducing the uncertainty in emission inventories and has led to improvements in air quality forecasting (Ma et al., 2019; Miyazaki et al., 2012b), since it would offer additional constraints on emission estimates through the improvements in related atmospheric fields, chemical reactions, and gas-particle transformations (Miyazaki and Eskes, 2013). Barbu et al. (2009) updated sulfur oxide (SO_x) emissions with SO2 and sulfate aerosol observations and found that simultaneous assimilation of both species had better performance than assimilating one of them alone.

The deviation in chemical initial condition (IC) is one of the important sources of error that affects the accuracy of emission inversion, because atmospheric inversion fully attributes the biases in simulated and observed concentrations to the deviations in emissions (Meirink et al., 2006; Peylin et al., 2005). The biases of concentrations would be compensated through unreasonable adjustment of pollution emissions without the optimization of ICs (Tang et al., 2013). Tang et al. (2011) reported that the simultaneous optimizations of the ICs of O_3, NO_x and volatile organic compounds (VOCs) and the emissions of NO_x and VOCs produced an overall better performance in ozone forecasts

than the adjustment in emissions only. Similar method of simultaneously optimizing chemical ICs and emissions were also applied to constraining emissions in many previous studies (Ma et al., 2019; Miyazaki et al., 2012a; Peng et al., 2018). Although a large improvement has been achieved, this method still has great limitations because the contributions from the emissions and the chemical ICs to the model's bias are difficult to distinguish (Jiang et al., 2017). In addition, in this method, the constraints of the chemical ICs with observations in each assimilation window make the emission inversions are independent between assimilation windows, means if the emission in one window is overestimated or underestimated, it cannot be transferred to the next window for further correcting and be compensated in the following windows. This may result in a systematic bias in the inverted emissions (Jiang et al., 2021).

Since 2013, China has deployed an air pollution monitoring network that publishes nationwide and real-time hourly surface atmospheric observations. This dataset provides an opportunity to improve emission estimates using DA. In this study, a regional multi- air pollutant assimilation system introducing 3DVAR and EnKF DA techniques is constructed to simultaneously assimilate various surface observations (e.g., CO, SO_2, NO_2, O_3, $PM_{2.5}$ and PM_{10}). Considering the possible shortcomings of the simultaneous optimization method (named as "one-step" method in this study) as metioned by Jiang et al. (2021), we adopted a "two-step" method (Sect. 3) in this system. Unlike the "one-step" method, the ICs of each DA window in the "two-step" method is simulated using the posterior emissions of the pervious DA window. The capability of RAPAS in reanalysis field generation and emission inversion estimation was evaluated. The robustness of the system was also investigated with different prior inventories, uncertainty settings of the prior emission, and observation errors. This paper is organized as follows: in Sect. 2, we introduce the DA system and the observation data, and in Sect. 3, we describe the experimental design. The results of the system performance and sensitivity tests are presented and discussed in Sect. 4, followed by the conclusions in Sect. 5.

2. Method and data

2.1 System description

2.1.1 Procedure of the assimilation system

A regional air pollutant assimilation system has been preliminarily constructed and successfully applied in our previous studies to optimize gridded CO and NO_x emissions (Feng et al., 2020a; Feng et al., 2020b). Herein, the system was further extended to simultaneously assimilate multiple species (e.g., CO, SO_2, NO_2, O_3, $PM_{2.5}$ and PM_{10}) and officially named as the Regional multi- Air Pollutant Assimilation System (RAPASv1.0). The RAPAS mainly includes three components: a regional chemical transport model (CTM), which is coupled offline and used to simulate the meteorological fields and atmospheric compositions, and the 3DVAR and ensemble square root filter (EnSRF) modules, which are used to optimize chemical ICs (Feng et al., 2018; Jiang et al., 2013b) and anthropogenic emissions (Feng et al., 2020a; Feng et al., 2020b), respectively. The introduction of 3DVAR mainly considers its great performance based on our previous study and lower computational cost during spin-up period in optimizing ICs. Additionally, it has been found that the 3DVAR method can obtain a better initial field than the EnKF method (Schwartz et al., 2014).

Based on above three components, the RAPAS is divided into two subsystems, namely the IC assimilation (IA) subsystem (CTM plus 3DVAR) and the emission inversion (EI) subsystem (CTM plus EnSRF). As shown in Figure 1, the IA subsystem is first run to optimize chemical ICs (Kleist et al., 2009; Wu et al., 2002) for the subsequent EI subsystem. In the IA subsystem, we do not need to distinguish the type of sources of the model-observation mismatch error. The EI subsystem runs cyclically with a "two-step" scheme. In the first step, the prior emissions ($\boldsymbol{X^b}$) are perturbed and put into the CTM model to simulate chemical concentration ensembles. The simulated concentrations of the lowest model level are then interpolated to the observation space according to the locations and times of the observations using the nearest neighbor interpolation method. The prior emissions ($\boldsymbol{X^b}$), simulated observations and real

observations are entered into the EnSRF module to generate the optimized emissions ($\boldsymbol{X^a}$). In the second step, the optimized emissions are entered into the CTM model again to generate the initial fields of the next DA window. Meanwhile, the optimized emissions are transferred to the next window as the prior emissions. Different from the "one-step" scheme, this "two-step" scheme needs to run the CTM model twice, which is time consuming, but it could transfer the potential errors of the inverted emissions in one DA window to the next for further correction. The benefit of this scheme will be further presented in Sect. 4.3.

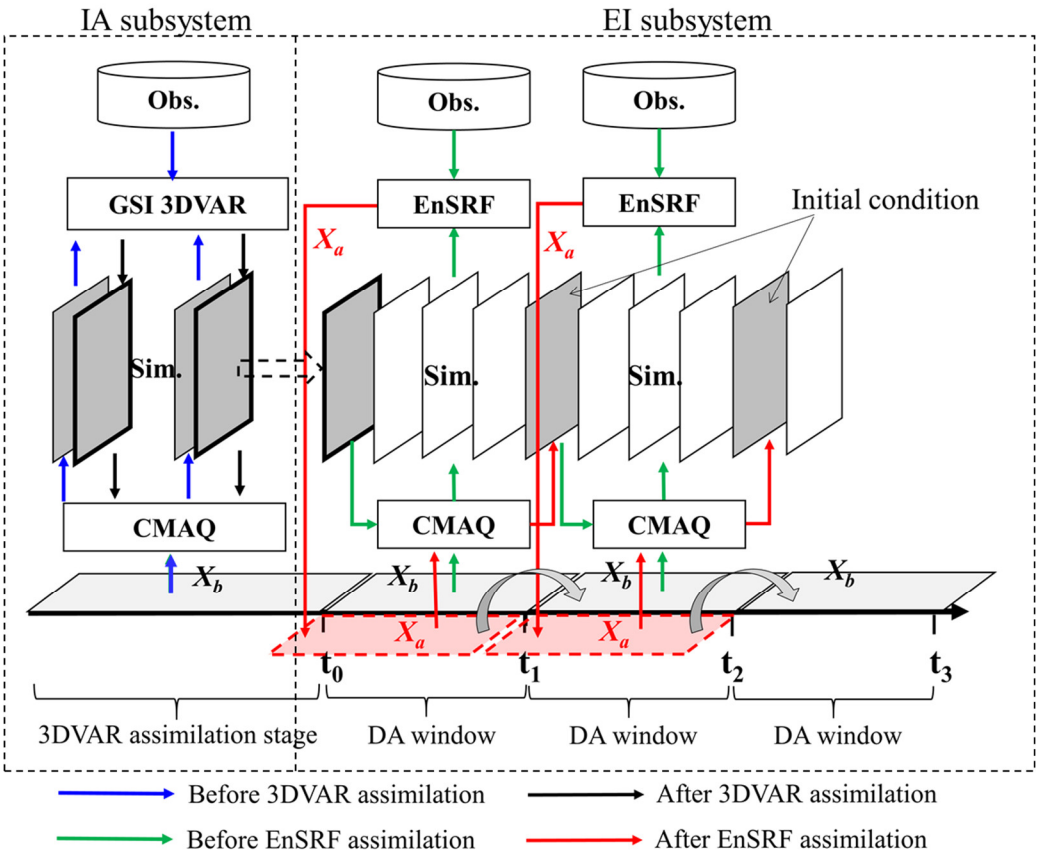

Figure 1. The composition and flow chart of RAPAS. The $\mathbf{x_a}$ and $\mathbf{x_b}$ represent the prior and posterior emissions. The 3DVAR assimilation stage lasts 5 days with data input frequency of 6 hours, and the DA window in the EI subsystem is set to 1 day.

2.1.2 Atmospheric transport model

The regional chemical transport model of WRF/CMAQ was adopted in this study. CMAQ is a regional 3-D Eulerian atmospheric chemistry and transport model with a

"one-atmosphere" design developed in the US Environmental Protection Agency (EPA). It can address the complex interactions among multiple pollutants/air quality issues simultaneously. CMAQ was driven by the WRF model, which is a state of the art mesoscale numerical weather prediction system designed for both atmospheric research and meteorological field forecasting. In this study, WRF version 4.0 and CMAQ version 5.0.2 were adopted. The WRF simulations were performed with a 36-km horizontal resolution on 169 × 129 grids, and it covers the whole of mainland of China (Figure 2). This spatial resolution has been widely adopted in regional simulations and can provide good simulations of the spatiotemporal variations of air pollutants (Mueller and Mallard, 2011; Sharma et al. 2016). In the vertical direction, there are 51 sigma levels on sigma-pressure coordinates extending from the surface to 100 hPa. The underlying surface of urban and built-up land was replaced by the MODIS land cover retrieval of 2016 to adapt to the rapid expansion of urbanization. The CMAQ model is run with the same domain but with three grid cells removed from each side of the WRF domain. There are 15 layers in the CMAQ vertical coordinate, which were interpolated from the 51 WRF layers.

The meteorological initial and lateral boundary conditions are both provided by the Final (FNL) Operational Global Analysis data of the National Center for Environmental Prediction (NCEP) with a 1° × 1° resolution at 6-h intervals. The chemical lateral boundary conditions and chemical ICs in the IA subsystem come from the background profiles. As mentioned above, in the EI subsystem, the chemical IC in the first window is provided by the IA subsystem, and in the following windows, it is forward simulated using optimized emission from the previous window. The Carbon Bond 05 with updated toluene chemistry (CB05tucl) and the 6th generation aerosol module (AERO6) are chosen as the gas-phase and aerosol chemical mechanisms, respectively (Appel et al., 2013; Sarwar et al., 2012). Detailed physical and chemical configurations are listed in Table 1.

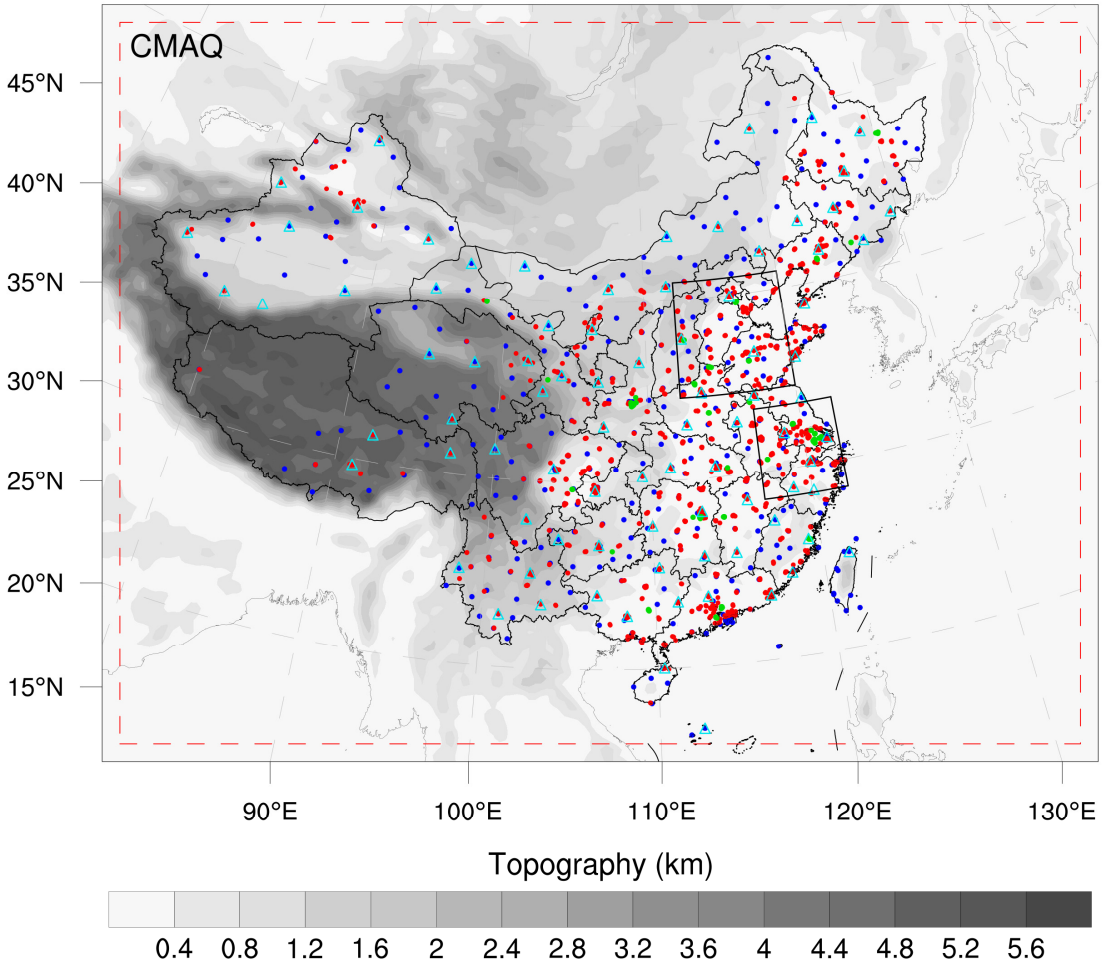

Figure 2. Model domain and observation network. The red dashed frame depicts the CMAQ computational domain; the blue dots represent the surface meteorological measurement sites; the turquoise triangles represent the sounding sites; and the red and green dots represent the air pollution measurement sites. Observations of all sites are assimilated in the 3DVAR subsystem, while observations of city sites where red dots are averaged are used for assimilation and where green dots are averaged are used for independent evaluation in EI subsystem; the boxed subregions are the North China Plain (NCP) and Yangtze River Delta (YRD); and the shaded area depicts the topography.

Table 1. Configuration options of WRF/CMAQ

WRF		CMAQ	
Parameter	Scheme	Parameter	Scheme
Microphysics	WSM6	Horizontal/Vertical advection	yamo/wrf
Longwave	RRTM	Horizontal/Vertical diffusion	multiscale/acm2
Shortwave	Goddard	Deposition	m3dry
Boundary layer	ACM	Chemistry solver	EBI
Cumulus	Kain-Fritsch	Photolysis	phot_inline
Land-surface	Noah	Aerosol module	AERO6
Surface layer	Revised	Cloud module	cloud_acm_ae6
Urban canopy	No	Gas-phase chemistry	CB05tucl

2.1.3 3DVAR assimilation algorithm

The Grid-point Statistical Interpolation (GSI) developed in the US National Centers for Environmental Prediction (NCEP) was employed in this study. Building upon the work of Liu et al. (2011), Jiang et al. (2013b) and Feng et al. (2018), we extended it to simultaneously assimilate multiple species (including CO, SO_2, NO_2, O_3, $PM_{2.5}$, and PM_{10}) and first used individual aerosol species of $PM_{2.5}$ as analysis variables within the GSI/WRF/CMAQ framework. Additional work includes the construction of surface air pollutant observation operators, the updating of observation errors, and the statistics of background error covariance for the analysis variables. Moreover, the data interface was also modified to read/write the CMAQ output/input file directly, which is easy to implement.

In the sense of a minimum analysis error variance, the 3DVAR algorithm optimizes analysis fields with observations by iterative processes to minimize the cost function (J(x)) defined below:

$$\mathrm{J(x)} = \frac{1}{2}(\mathbf{x_a} - \mathbf{x_b})^T \mathbf{B}^{-1}(\mathbf{x_a} - \mathbf{x_b}) + \frac{1}{2}[H(\mathbf{x_a}) - \mathbf{y}]^T \mathbf{R}^{-1}[H(\mathbf{x_a}) - \mathbf{y}], \quad (1)$$

where $\mathbf{x_a}$ is a vector of the analysis field; $\mathbf{x_b}$ denotes the background field; **y** is the vector of observations; **B** and **R** are the background and observation error covariance matrices, respectively, representing the relative contributions to analysis; and *H* is the observation operator that maps the model variables to the observation space.

The analysis variables are the 3D mass concentrations of the pollution compositions (e.g., CO and sulfate) at each grid point. Hourly mean surface pollution observations within a 1 hour window of the analysis are assimilated. To assimilate the surface pollution observations, model-simulated compositions are first diagnosed at the observation locations. For gas concentrations that are directly used as analysis variables, data units need to be converted from ppm or ppb to mg m^{-3} or μg m^{-3} to match with observations. The model-simulated $PM_{2.5}$ and PM_{10} concentrations at the ground level are diagnosed as follows:

$$PM_{2.5} = f_i \times PM_i + f_j \times PM_j + f_k \times PM_k = \mathrm{OC} + \mathrm{EC} + SO_4^{2-} + NO_3^- + NH_4^+ + SEAS + AP_{2.5} \quad (2)$$

$$PM_{10} = PM_i + PM_j + PM_k = PM_{2.5} + PMC \quad (3)$$

where f_i, f_j, and f_k are the $PM_{2.5}$ fractions of the Aitken, accumulation, and coarse modes, respectively. These ratios are recommended as the concentrations of $PM_{2.5}$ and fine mode aerosols (i.e., Aitken plus accumulation) could differ because the $PM_{2.5}$ particles include small tails from the coarse mode in the CMAQ model (Binkowski and Roselle, 2003; Jiang et al., 2006). PM_i, PM_j, and PM_k represent the mass concentrations of the 3 modes in the CMAQ model. Seven aerosol species of $PM_{2.5}$, including organic carbon (OC), elemental carbon (EC), sulfate (SO_4^{2-}), nitrate (NO_3^-), ammonium (NH_4^+), sea salt (SEAS), and fine-mode unspeciated aerosols ($AP_{2.5}$), and additional coarse PM_{10} (PMC) are extracted as analysis variables, which are updated by the $PM_{2.5}$ and PMC observations, respectively. Before the calculation of equation (1) within the GSI, the analysis variables are bilinearly interpolated in the horizontal direction to the observation locations.

The computation of background error covariance (**B**) is generally costly and difficult when a high-dimensional numerical model is used. For simplification, **B** is represented as a product of spatial correlation matrices and standard deviations (SDs):

$$\mathbf{B} = \mathbf{DC}\boldsymbol{D}^{\boldsymbol{T}} \tag{4}$$

$$\mathbf{C} = \boldsymbol{C}_{\boldsymbol{x}} \otimes \boldsymbol{C}_{\boldsymbol{y}} \otimes \boldsymbol{C}_{\boldsymbol{z}} \tag{5}$$

where **D** is the background error SD matrix, **C** is the background error correlation matrix, $\otimes$ denotes the Kronecker product, and $\boldsymbol{C}_{\boldsymbol{x}}$, $\boldsymbol{C}_{\boldsymbol{y}}$, and $\boldsymbol{C}_{\boldsymbol{z}}$ denote three one-dimensional correlation submatrices in the longitude, latitude, and vertical coordinate directions, respectively. $\boldsymbol{C}_{\boldsymbol{x}}$ and $\boldsymbol{C}_{\boldsymbol{y}}$ are assumed to be isotropic horizontally such that can be represented using a Gaussian function. The correlation between any two points x_i and x_j in the horizontal can be expressed as follows:

$$\mathrm{c}(x_i,\ x_j) = e^{-\frac{(x_i - x_j)^2}{2L^2}} \tag{6}$$

where L is the horizontal correlation scale, which is estimated using the proxy of the background error (Figure 3). The vertical correlation matric $\boldsymbol{C}_{\boldsymbol{z}}$ is directly estimated from the model background field since $\boldsymbol{C}_{\boldsymbol{z}}$ is only an $n_z \times n_z$ (here, n_z=15) matrix.

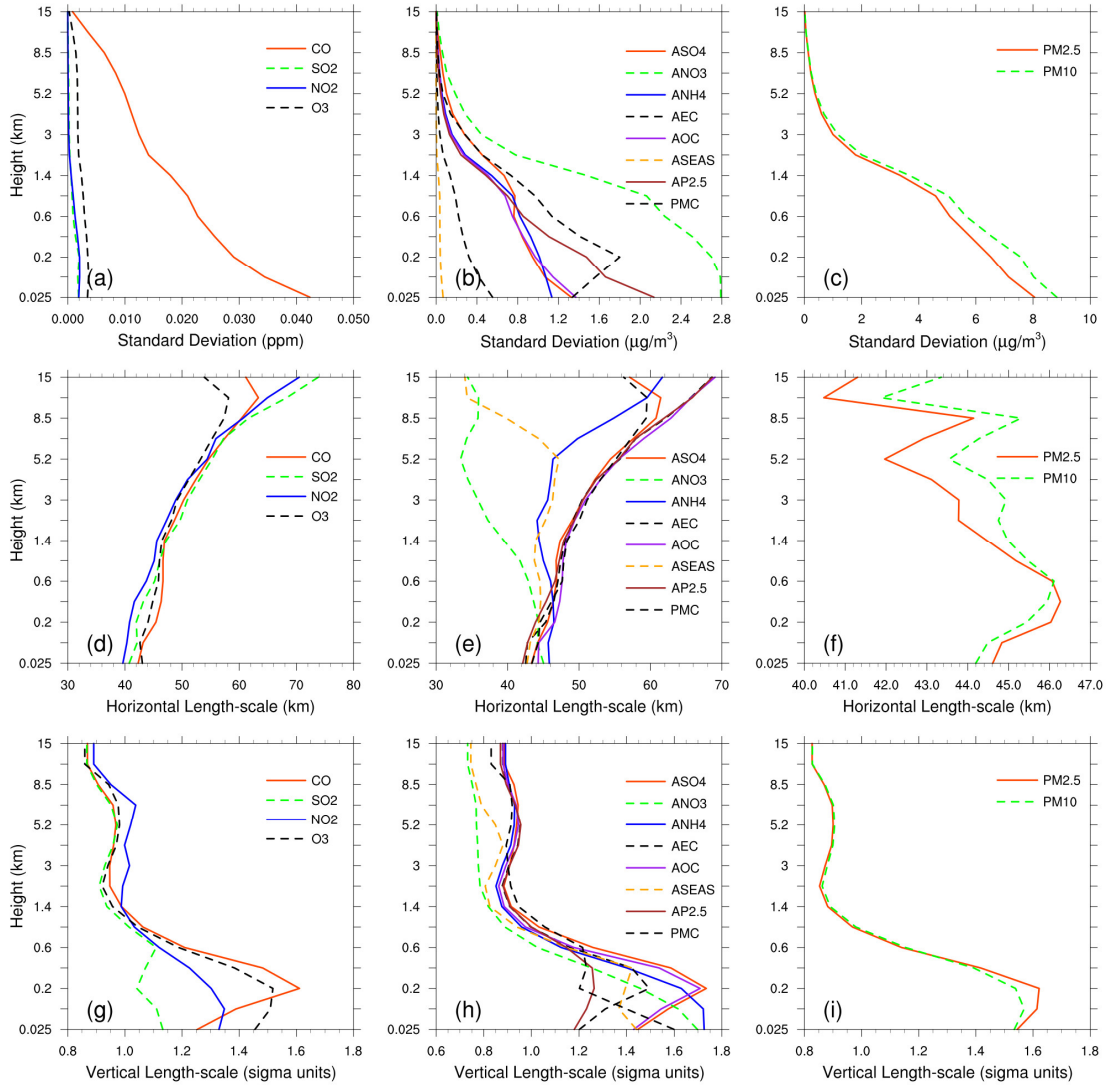

Figure 3. Vertical profiles of standard deviations (top, μg m^{-3}), horizontal length scale (middle, km) and vertical length scale (bottom, km) for CO, SO_2, NO_2, O_3, sulfate, nitrate, ammonium, EC, OC, sea salt, unspeciated aerosols (AP2.5), PMC, $PM_{2.5}$ and PM_{10}.

To estimate these matrices, the "NMC" method is used here to compute **B** for each variable by taking the differences between forecasts of different lengths valid at the same time (Parrish and Derber, 1992; Rabier et al., 1998). Differences between 24- and 12-h WRF/CMAQ forecasts of 60 pairs (two pairs a day) of analysis variables valid at either 0000 or 1200 UTC over November 2016 are used. The horizontal and vertical length scales of the correlation matrices are estimated by recursive filters (Purser et al., 2003). The vertical distribution of background error SDs is shown in Figure 3, which

varies with height and species. The vertical profile of the background error SDs corresponds to the vertical concentration distribution. This means that higher concentrations tend to have larger background error SDs (e.g., CO and nitrate). These SDs exhibit a common reduction with height, especially at the top of the boundary layer. The horizontal correlation of background error determines the propagation of observation information in this direction, while vertical correlation determines the vertical extension of such increments. For gaseous pollutants and most individual aerosol components, the horizontal length scales increase with height, while for the total particulate matter (i.e., PM2.5 and PM10), the scales increase with height in the boundary layer and decrease with height in the free troposphere. The ground-level scale generally spreads 40-45 km for all control variables on average. The vertical length scale of most species increases first and then decreases with height, which may be related to the vertical mixing (Kahnert, 2008) and stack emissions at about 200 m height.

2.1.4 EnKF assimilation algorithm

In EnKF, the time-dependent uncertainties of the state variables are estimated using a Monte Carlo approach through an ensemble. Uncertainty can be propagated with linear or nonlinear dynamic models (flow-dependent background error covariance) by simply implementing ensemble simulations. The EnSRF algorithm introduced by Bierman (1977) and Maybeck (1979) is used to constrain pollution emissions in this study. EnSRF is a deterministic EnKF that obviates the need to perturb observations, which has a higher computational efficiency and a better performance (Sun et al., 2009).

The perturbation of prior emissions represents the uncertainty. We implement additive emission adjustment methods, which are calculated using the following function.

$$\boldsymbol{X_i^b} = \boldsymbol{X_0^b} + \boldsymbol{\delta X_i^b}, \text{ i} = 1, 2, ..., \text{N} \quad (7)$$

where $\boldsymbol{b}$ represents the background (prior) state, i is the identifier of the perturbed samples, N is the ensemble size, which was set to 40 in consideration of a tradeoff between the computation cost and inversion accuracy (Figure S1), and $\delta\boldsymbol{X_i^b}$ represents the randomly perturbed samples that are added to the prior emissions $\boldsymbol{X_0^b}$ to produce

ensemble samples of the inputs $\boldsymbol{X_i^b}$. $\delta\boldsymbol{X_i^b}$ is drawn from Gaussian distributions with a mean of zero and the standard deviation of the prior emission uncertainty in each grid. The state variables of the emissions include CO, SO_2, NO_x, primary $PM_{2.5}$ ($PPM_{2.5}$) and PMC. We used variable localization to update the analysis, which means that the covariance among different state variables was not considered, and the emission of one species was only constrained with its corresponding air pollutant observation. This method has been widely used in chemical data assimilation systems to avoid spurious correlations among species. (Ma et al., 2019; Miyazaki et al., 2012b).

After obtaining an ensemble of state vectors (prior emissions), ensemble runs of the CMAQ model are conducted to propagate these errors in the model with each ensemble sample of state vectors. Combined with observational vector $\boldsymbol{y}$, the state vector is updated by minimizing the analysis variance:

$$\overline{\boldsymbol{X^a}} = \overline{\boldsymbol{X^b}} + \mathbf{K}(\mathbf{y} - \boldsymbol{H}\overline{\boldsymbol{X^b}}) \tag{8}$$

$$\mathbf{K} = \boldsymbol{P^b H^T}(\boldsymbol{H P^b H^T} + \boldsymbol{R})^{-1} \tag{9}$$

$$\boldsymbol{P^b} = \frac{1}{N-1}\sum_{i=1}^{N}(\boldsymbol{X_i^b} - \overline{\boldsymbol{X}}^{\boldsymbol{b}})\,(\boldsymbol{X_i^b} - \overline{\boldsymbol{X}}^{\boldsymbol{b}})^T \tag{10}$$

$$\delta\boldsymbol{X_i^a} = \delta\boldsymbol{X_i^b} - \widetilde{\boldsymbol{K}}\boldsymbol{H}\delta\boldsymbol{X_i^b} \tag{11}$$

While employing sequential assimilation and independent observations, $\widetilde{\boldsymbol{K}}$ is calculated as follows:

$$\widetilde{\boldsymbol{K}} = \left(1 + \sqrt{\boldsymbol{R}/(\boldsymbol{H P^b H^T} + \boldsymbol{R})}\right)^{-1}\mathbf{K} \tag{12}$$

where $\overline{\boldsymbol{X}}^{\boldsymbol{b}}$ represents the mean of the ensemble samples; $\boldsymbol{H}$ is the observation operator that maps simulated concentrations from model space to observation space; $\boldsymbol{y} - \boldsymbol{H}\overline{\boldsymbol{X^b}}$ reflects the differences between the simulated and observed concentrations; $\boldsymbol{P^b}$ is the ensemble-estimated background (a priori) error covariance; $\boldsymbol{P^b H^T}$ contains the response of the uncertainty in the simulated concentrations to the uncertainty in emissions; $\boldsymbol{K}$ is the Kalman gain matrix of the ensemble mean depending on the $\boldsymbol{P^b}$

and observation error covariance $\boldsymbol{R}$, representing the relative contributions to analysis; and $\widetilde{\boldsymbol{K}}$ is the Kalman gain matrix of the ensemble perturbation, which is used to calculate emission perturbations after inversions $\delta \boldsymbol{X}_i^{\boldsymbol{a}}$. The ensemble mean $\overline{\boldsymbol{X^a}}$ of the analyzed state is taken as the best estimate of the emissions.

With large volumes of site observations that are recorded at a much higher resolution than the model grid spacing, there would be significant correlated or fully consistent model-data mismatch errors in one cluster, resulting in excessive adjustments and deteriorated model performances (Houtekamer and Mitchell, 2001). To reduce the horizontal observation error correlations and the influence of representativeness errors, a "super-observation" approach combining multiple noisy observations located within the same grid and assimilation window is developed based on optimal estimation theory (Miyazaki et al., 2012a). Previous studies have demonstrated the necessity of data-thinning and dealiasing errors (Feng et al., 2020b; Zhang et al., 2009a). The super-observation y_{new}, super-observation error r_{new} and corresponding simulation $x_{new,i}$ of the *i*th sample are calculated as follows:

$$1/r_{new}^2 = \sum_{j=1}^{m} 1/r_j^2 \tag{13}$$

$$y_{new} = \sum_{j=1}^{m} w_j\, y_j / \sum_{j=1}^{m} w_j \tag{14}$$

$$x_{new,i} = \sum_{j=1}^{m} w_j\, x_{ij} / \sum_{j=1}^{m} w_j \tag{15}$$

where j is the identifier of m observations within a super-observation grid; r_j is the observational error of actual *j*th observation y_j; x_{ij} represents a simulated concentration using the *i*th prior emission sample corresponding to the *j*th observation; and $w_j = 1/r_j^2$ is the weighting factor. The super-observation error decreases as the number of observations used within a super-observation increases. This method has been used in our previous inversions using surface-based (Feng et al., 2020b) and

satellite-based (Jiang et al., 2021) observations.

In this study, the DA window was set to 1 day because the model needs a longer time to integrate emission information into the concentration ensembles (Ma et al., 2019). Due to the "super-observation" approach, only one assimilation is needed in one assimilation window. In addition, due to the complexity of hourly emissions, it is very difficult to simulate hourly concentrations that can match the observations well. Although a longer DA window could allow more observations to constrain the emission change of one grid, the spurious correlation signals of EnKF would attenuate observation information with time (Bruhwiler et al., 2005; Jiang et al., 2021). Kang et al. (2012) conducted OSSEs and demonstrated that due to the errors of transport and increase the spurious correlation, a longer DA window (e.g., 3 weeks) would cause the analysis system to blur out the essential emission information far away from the observation. Therefore, daily mean simulations and observations are used in the EnSRF algorithm, and daily emissions are optimized in this system.

EnKF is subject to spurious correlations due to the limited number of ensembles when it is applied in high-dimensional atmospheric models, which can cause rank deficiencies in the estimated background error covariance and filter divergence, and further degrade analyses and forecasts (Wang et al., 2020). Covariance localization is performed to reduce spurious correlations caused by the finite ensemble size (Houtekamer and Mitchell, 2001). Covariance localization preserves the meaningful impact of observations on state variables within a certain distance (cutoff radius) but limits the detrimental impact of observations on remote state variables. The localization function of Gaspari and Cohn function (Gaspari and Cohn, 1999) is used in this system, which is a piecewise continuous fifth-order polynomial approximation of a normal distribution. The optimal localization scale is related to the ensemble size, assimilation window, dynamic system, and lifetime of a chemical species in the atmosphere. CO, SO_2 and $PM_{2.5}$ are rather stable in atmosphere, with a lifetime more than 1 day. According to the averaged wind speed (3.3 m/s, Table 4) and the length of DA window, their localization scales are set to 300 km. In addition, NO_2 is rather reactive, with a

lifetime of approximately 10 hours in winter (de Foy et al., 2015), and PMC, which is mainly from local sources, its residence time in the atmosphere is also short due to the rapid deposition rate (Clements et al., 2014; Clements et al., 2016; Hinds, 1982). Their localization scales are set to 150 km and 250 km, respectively.

2.2 Prior emissions and uncertainties

The anthropogenic emissions over China were taken from the 2016 Multi-resolution Emission Inventory for China (MEIC 2016) (Zheng et al., 2018), while those over the other regions of East Asia were obtained from the mosaic Asian anthropogenic emission inventory (MIX) (Li et al., 2017). The spatial resolutions of both the MEIC and MIX inventories are 0.25° × 0.25°, and they are both downscaled to match the model grid spacing of 36 km. The spatial distributions of the CO, SO_2, NO_x, $PPM_{2.5}$ and PMC emissions are shown in Figure 12. The daily emission inventory, which was arithmetic averaged from the combined monthly emission inventory, was directly used in the EI subsystem and employed as the prior emission of the first DA window in the EI subsystem (Figure 1). During the simulations, the daily emissions were further converted to hourly emissions. For all the species emitted from area sources, we converted them to hourly using a same diurnal profile (Figure S2), and for the point source, we assumed that there was no diurnal change. MEIC 2012 was used as an alternative a priori over China to investigate the impact of different prior emissions on the optimized emissions. The Model of Emissions of Gases and Aerosols from Nature (MEGAN) (Guenther et al., 2012) was used to calculate time-dependent biogenic emissions. It was also driven by the WRF model in this study. Biomass burning emissions were not included because they have little impact across China during the study period (Zhang et al., 2020).

During the inversion cycles, the inverted emissions of different members converge gradually, and the ensemble-estimated error covariance matrix is arithmetically likely to be underestimated. To avoid this, considering the compensation of model errors and comparable emission uncertainties from one day to the next, we impose the same uncertainty on emissions at each DA window. As mentioned above, the optimized

emissions of the current DA window are transferred to the next DA window as prior emissions. The technology-based emission inventory developed by Zhang et al. (2009b), basically using the same method as MEIC, shows that the emissions of PMC and $PPM_{2.5}$ have the largest uncertainties, followed by CO, and finally SO_2 and NO_x. Therefore, the uncertainties in this study are set to 40%, 40%, 30%, 25%, and 25%. However, previous studies have shown that the inversely estimated CO and PMC emissions could exceed 100% higher than the bottom-up emissions (MEIC) in certain areas (Feng et al., 2020b; Ma et al., 2019). According to the extent of underestimation, we set an uncertainty of 100% for both the CO and PMC emissions at the beginning of the three DA windows to quickly converge the emissions. The mean emission analysis is generally minimally sensitive to the uncertainty setting in our assimilation cycle method (Feng et al., 2020; Gurney et al., 2004; Miyazaki et al., 2012a) because the inversion errors of the current window could be transferred to the next window for further optimization (Sect. 4.3).

2.3 Observation data and errors

Hourly averaged surface CO, SO_2, NO_2, O_3, $PM_{2.5}$ and PM_{10} observations from 1504 national control air quality stations were assimilated in this system, which were obtained from the Ministry of Ecology and Environment of the People's Republic of China (http://106.37.208.233:20035/, last access: 25 June 2020). These sites are distributed over most of central and eastern China and become denser near metropolitan areas (see Figure 2). Value-range and time-continuity checks were performed to ensure data quality. Value-range checks were mainly performed to eliminate unrealistic or unrepresentative observations. Only observations within the subjectively selected threshold range were assimilated (Table 2). A time-continuity check was performed to eliminate gross outliers and a sudden anomaly using a function of $max(|O(t) - O(t \pm 1)|) \leq f(t)$, where $O(t)$ and $O(t \pm 1)$ represent observations at time t and $t \pm 1$, respectively, and $f(t) = T_a + T_b \times O_t$. That means that both concentration differences between time *t* and time *t+1* and *t-1* should be less than $f(t)$. T_b is fixed to 0.15, and the section of T_a is given in Table 2, which is determined empirically according to the time series change of concentration at each site. It should be noted that,

to avoid potential cross-correlations, we assimilated $PM_{2.5}$ and PMC. Additionally, in the EI subsystem, the observations within each city were averaged to thin the data density, reduce the error correlation and increase the spatial representation (Houtekamer and Mitchell, 2001; Houtekamer and Zhang, 2016). Finally, 336 city sites are available across the mainland of China, in which 311 cities' data were selected for assimilation and the remaining 25 were selected for independent validation (Figure 2). In the IA subsystem, due to the small horizontal correlation scale (Figure 3), to obtain more extensive observation constraints, all site observations were assimilated to provide a good IC for the next emission inversion.

The observation error covariance matrix (***R***) includes both measurement and representation errors. The measurement error ε_0 is defined as follow:

$$\varepsilon_0 = ermax + ermin \times \Pi_0 \tag{16}$$

where $ermax$ is a base error, and Π_0 denotes the observed concentration. These parameters for different species are listed in Table 2, which are determined according to Chen et al. (2019), Feng et al., (2018) and Jiang et al. (2013b).

The representative error depends on the model resolution and the characteristics of the observation locations, which were calculated using the equations of Elbern et al. (2007) defined as follows:

$$\varepsilon_r = \gamma \varepsilon_0 \sqrt{\Delta l / L} \tag{17}$$

where γ is a tunable parameter (here, γ=0.5), Δl is the grid spacing (36 km), and L indicates the radius (here, 3 km for simplification) of influence area of an observation. The total observation error (r) is defined as follows:

$$r = \sqrt{{\varepsilon_0}^2 + {\varepsilon_r}^2} \tag{18}$$

Table 2. Parameters of quality control and measurement error

Parameter	CO mg m^{-3}	SO_2 μg m^{-3}	NO_2 μg m^{-3}	O_3 μg m^{-3}	$PM_{2.5}$ μg m^{-3}	PMC μg m^{-3}

value-range	0.1-12	1-800	1-250	1-250	1-800	1-900
time-continuity (T_a)	2.5	160	70	80	180	180
ermax	0.05	1	1	1	1.5	1.5
ermin	0.5%	0.5%	0.5%	0.5%	0.75%	0.75%

514

515 # 3 Experimental design

516 RAPAS was conducted according to the procedure and settings described in Sect. 2.
517 December is one of the months with most severe air pollution, while July is one of the
518 least polluted months in China. Therefore, this study mainly tested the performance of
519 the RAPAS system in these two months. For December, the IA subsystem was run from
520 26 to 31 November 2016 with a 6-hour interval cycling assimilation to optimize ICs
521 (ICDA). A better IC at 0000 UTC on December 1 can be obtained by 5-day high-
522 frequency cycling assimilation and atmospheric mixing. Then the EI subsystem was
523 run for December 2016 with a 1-day assimilation window to optimize emissions
524 (EMDA). For July, the system also operated in the same way as for December. It needs
525 to be noted that due to the stronger atmospheric oxidation, the lifetime of NO2 in July
526 is significantly shorter than that in December, thus we adopted a smaller localization
527 scale for NO2 (80 km). Both assimilation experiments use the combined prior emission
528 inventories of 2016 as described in Sect. 2.2, and the emission base year coincides with
529 the research stage. An Observing Systems Simulation Experiment (OSEE) was
530 conducted to evaluate the performance of the RAPAS system, which has been widely
531 used in previous assimilation systems development (Daley, 1997). In the OSSE
532 experiment, we used the MEIC 2016 inventory as a "true" emission, and reduced the
533 "true" emission by 30% over the mainland of China as a prior emission. The simulations
534 simulated using the "true" emission and sampled according to the locations and times
535 of the real observations were used as artificial observations. The observation errors are
536 the same as those in EMDA. To evaluate the IC improvements from the IA subsystem,

an experiment without 3DVAR (NODA) is conducted with the same meteorological fields and physical and chemistry parameterization settings as those of the ICDA. To evaluate the posterior emissions of the EI subsystem, two parallel forward modeling experiments are performed for December 2016, namely, a control experiment (CEP) with prior (MEIC 2016) emissions and a validation experiment (VEP) with posterior emissions. Both experiments use the same initial field at 0000 UTC on December 01 generated through the IA subsystem. Similar to the above, the only differences between CEP and VEP are emissions. Table 3 gives a summary of different emission inversion experiments conducted in this study.

To investigate the robustness of our system, 8 sensitivity tests (from EMS1 to EMS8, see Table 3) are performed. These experiments are all based on EMDA. In EMS1, rather than forward simulated using the optimized emissions of the previous DA window in EMDA, the initial fields of each DA window were first taken from forward simulation with the prior emissions of the previous DA window, and then optimized using the 3DVAR algorithm and the observations at the corresponding moment as mentioned in Sect. 2.3. The objective of this experiment is to investigate the advantages of the "two-step" calculation scheme in the EI subsystem as introduced in Sect. 2.1. EMS2 uses MEIC 2012 as the original prior emission in China, aiming to investigate the impact of different prior inventories on the estimates of emissions. Four other experiments, namely EMS3-6, aim to test the impact of different prior uncertainty settings, in which, the prior uncertainties are reduced by -50% and -25%, and increased by 25% and 50%, respectively. EMS7 aims to evaluate the impact of observation errors on emission estimates, in which all the observation errors are magnified twice. The last EMS8 experiment aims to evaluate the impact of IC optimization of the first window on emission estimates, in which the ICs were taken from a 5-day spin-up simulation. Eight forward modeling experiments (VEP1, VEP2, …, VEP8) were also performed with posterior emissions of EMS1 to EMS8 to evaluate their performances, respectively.

565 **Table 3**. Emission inversion and sensitivity experiments conducted in this study

Exp. Type	Exp. Name	Period	IC of the first DA Window	ICs of the subsequent DA window	Emission
Assimilation	EMDA	1-31 December	0000 UTC on December 1, taken from ICDA	Forecast with posterior emissions in the previous window	MEIC 2016 for December (the first DA window), optimized emissions of the previous window (other DA windows)
	OSSE	1-31 December	The same as EMDA	The same as EMDA	The same as EMDA, but with a decrease of 30% for CO, SO_2, NO_x, $PPM_{2.5}$, and PMC
Sensitivity	EMS1	1-31 December	The same as EMDA	Forecast with prior emissions in the previous window and 3DVAR assimilation	The same as EMDA
	EMS2	1-31 December	The same as EMDA	The same as EMDA	The same as EMDA, but for EMIC 2012
	EMS3-6	1-31 December	The same as EMDA	The same as EMDA	The same as EMDA, but with a ± 25% or ± 50% of default uncertainty
	EMS7	1-31 December	The same as EMDA	The same as EMDA	The same as EMDA, but with a +100% of default observation errors
	EMS8	1-31 December	0000 UTC on December 1, taken from ICNO	The same as EMDA	The same as EMDA

566

567

568

569

4 Results

4.1 Evaluations

4.1.1 Simulated meteorological fields

In the RAPAS system, the inversion approach attributes all the biases between the simulated and observed concentrations to the emissions. The meteorological fields dominate the physical and chemical processes of the air pollutants in the atmosphere, and thus their simulation accuracy would significantly affect the estimates of emissions in this study. To quantitatively evaluate the performance of the WRF simulations, the mean bias (BIAS), root mean square error (RMSE), and correlation coefficient (CORR) were calculated against the surface meteorological observations measured at 400 stations and the planetary boundary layer height (PBLH) calculated using the sounding data at 92 sites. The surface observations were obtained from the National Climate Data Center (NCDC) integrated surface database (http://www.ncdc.noaa.gov/oa/ncdc.html, last access: 25 October 2021), and the sounding data were obtained from the website of the University of Wyoming (http://weather.uwyo.edu/upperair/sounding.html, last access: 10 March 2022). The sounding data are in 12 hours interval. The observed PBLH were calculated using the sound data through the bulk Richardson number method (Richardson et al., 2013). The spatial distribution of the meteorological stations is shown in Figure 2. The simulated temperature at 2 m (T2), relative humidity at 2 m (RH2), wind speed at 10 m (WS10), and PBLH from 26 November to 31 December 2016 are evaluated against the observations. Table 4 summarizes the statistical results of the evaluations of the simulated meteorological parameters. Overall, the T2, RH2 and PBLH are slightly underestimated, with biases of -0.1 ℃, -3.8% and -41.1 m, respectively. The CORRs are approximately 0.98 for T2, 0.94 for RH2 and 0.90 for PBLH, showing good consistency between the observations and simulations. The WS10 is overestimated, with a bias of 0.7 m/s and an RMSE of 0.8 m/s, but is better than many other studies (Chen et al., 2016; Jiang et al., 2012a; Jiang et al., 2012b). Therefore, WRF can generally reproduce the meteorological conditions sufficiently in

terms of their temporal variation and magnitude over China, which is adequate for our inversion estimation.

Table 4. Statistics comparing the simulated and observed 10-m wind speed (WS10), 2-m temperature (T2), and 2-m relative humidity (RH2), and planetary boundary layer height (PBLH).

Variable Met.	No. of sites	Mean Obs.	Mean Sim.	BIAS	RMSE	CORR
WS10 (m/s)	400	2.6	3.3	0.7	0.8	0.72
T2 (°C)	400	2.9	2.8	-0.1	0.7	0.98
RH2 (%)	400	66.3	62.6	-3.8	5.2	0.94
PBLH (m)	92	267.5	226.4	-41.1	50.4	0.90

* BIAS, mean bias; RMSE, root mean square error; CORR, correlation coefficient

4.1.2 Initial fields

Figure 4 shows the evaluations of the analyzed concentrations of the 6 species against surface observations. For comparison, the evaluations of the simulations without 3DVAR (NODA) are also shown in Figure 4. The simulations of the NODA experiment (red dots) are scattered on both sides of a central line, as large systematic biases remain across many measurement sites. Conversely, the ICDA experiment (blue dots) shows much better agreement with observations than those from NODA. The statistics show that there are large systematic biases in the NODA simulations, with large RMSEs and small CORRs for all species, especially for CO and PMC. After the assimilation of surface observations, the RMSE of CO decreases to 0.7 mg m^{-3}, and those of SO_2, NO_2, O_3, $PM_{2.5}$ and PMC decrease to 22.0, 12.0, 9.6, 20.5 and 19.6 μg m^{-3}, respectively, with respective reduction rates of 50.0%, 73.1%, 61.0%, 64.7%, 69.5%, and 60.8% compared to the ones of the NODA (Table 5). The CORRs of ICDA increase by 290.0%, 291.3%, 55.4%, 87.2%, 130.0% and 214.8% to 0.78, 0.90, 0.87, 0.88, 0.92 and 0.85, respectively. These statistics indicate the initial fields of the ground level have been significantly improved. However, due to the lack of observations, we still do not know

the simulation bias in the upper-middle boundary layer. Although concentrations at high altitudes can be constrained by ground-based observations through vertical correlations, the effect is limited, so the bias is still non-negligible.

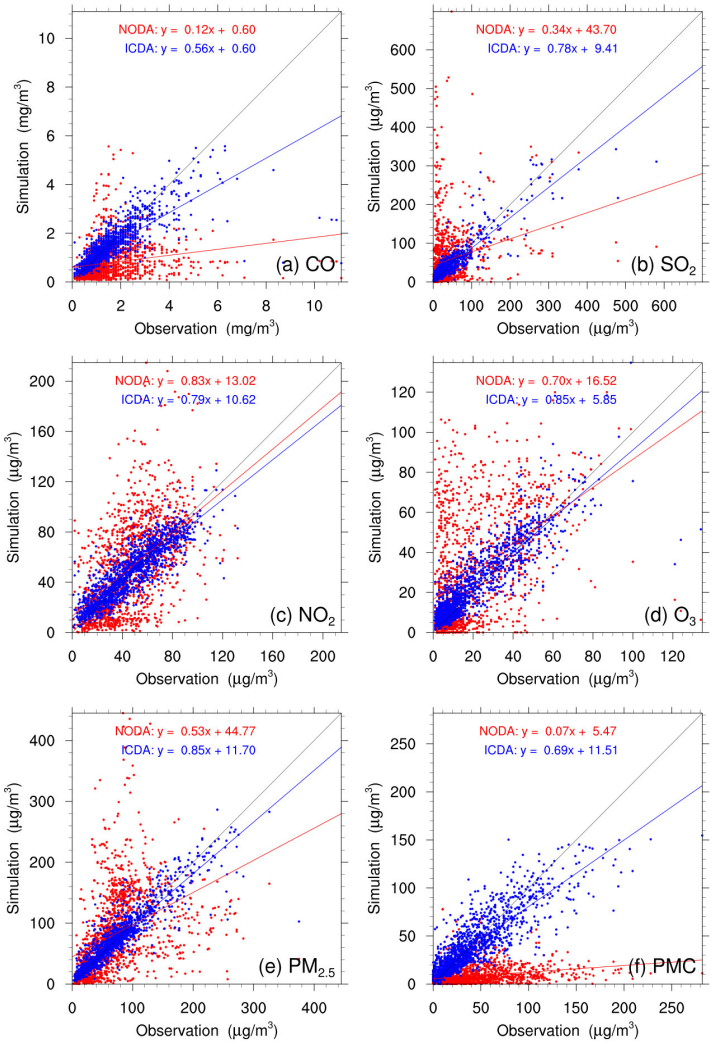

Figure 4. Scatter plots of simulated versus observed (a) CO, (b) SO_2, (C) NO_2, (d) O_3, (e) $PM_{2.5}$ and (f) PMC mass concentrations at 0000 UTC on December 1 initializations from the background (red) and analysis (blue) fields.

Table 5. Comparisons of the surface CO, SO_2, NO_2, O_3, $PM_{2.5}$ and PMC mass concentrations from the control and assimilation experiment against observations aggregated over all analysis times. CO unit: mg m^{-3}; others units: μg m^{-3}.

Species	Exp. Name	Mean Obs.	Mean Sim.	BIAS	RMSE	CORR
CO	NODA	1.5	0.8	-0.7	1.4	0.20
	ICDA		1.5	-0.1	0.7	0.78
SO_2	NODA	36.3	56.0	19.7	81.7	0.23
	ICDA		37.8	1.5	22.0	0.90
NO_2	NODA	45.8	51.1	5.3	30.8	0.56
	ICDA		47.0	1.1	12.0	0.87
O_3	NODA	20.5	30.8	10.4	27.2	0.47
	ICDA		23.3	2.8	9.6	0.88
$PM_{2.5}$	NODA	70.9	82.2	11.3	67.3	0.40
	ICDA		71.8	0.9	20.5	0.92
PMC	NODA	43.5	8.5	-35.0	50.0	0.27
	ICDA		41.6	-1.9	19.6	0.85

* BIAS, mean bias; RMSE, root mean square error; CORR, correlation coefficient

4.1.3 Posterior emissions

Due to mismatched spatial scales, it is difficult to directly evaluate the optimized emissions against observations. Generally, we indirectly validate them by comparing the forward simulated concentrations using the posterior emissions against atmospheric measurements (e.g., Jiang et al. (2014), Jin et al. (2018), and Peters et al. (2007)). Figure 5 shows the spatial distributions of the mean biases between the simulated gaseous pollutants using prior and posterior emissions and assimilated observations. In the CEPs, for each species, the distribution of biases is similar to the increments in background fields constrained through 3DVAR as shown in Figure S3. For example, almost all sites have large negative biases for CO, while for SO_2 and NO_2, positive biases are mainly distributed over the North China Plain (NCP), Yangtze River Delta (YRD), Sichuan Basin (SCB) and Central China, and negative biases are over the rest of the areas. After constraining with observations, the biases of all the 3 gaseous air pollutants are

significantly reduced in most sites. For CO, the biases at 62% of the sites decreased to absolute values less than 0.2 mg m^{-3}, and for SO_2 and NO_2, the biases at 52% and 47% of the sites were within ±4 μg m^{-3}. However, large negative biases are still observed in part of western Chinas, indicating that the uncertainties of the posterior emissions are still large in western China, which may be attributed to the large biases in prior emissions and to the relatively limited observation. Overall, the statistics show that there are different levels of improvements at 92%, 85% and 85% of the total 311 assimilation sites for CO, SO_2 and NO_2, respectively. The small amount of sites with worse performance may be related to the overadjusted emissions by EI or contradictory adjustments caused by opposite biases in adjacent areas.

Table 6 lists the statistical results of the evaluations averaged over the whole mainland of China. For CO, the mean bias is -0.8 mg m^{-3} with the prior emissions, while it substantially reduces to -0.1 mg m^{-3} with a reduction rate of 89.6% when simulating with the posterior emissions. Additionally, the RMSE decreases by 48.1% from 1.08 to 0.56 mg m^{-3}, and the CORR increases by 76.1% from 0.46 to 0.81. For SO_2 and NO_2, the regional mean biases slightly increase as the positive/negative biases among different sites might be offset. However, the RMSEs decrease to 17.7 and 12.3 μg m^{-3}, respectively, which are 58.3% and 50.8% lower than those of CEPs, and the CORRs increase by 125.6% and 35.4%, both reaching up to 0.88, indicating that EI has significantly improved the NO_x and SO_2 emission estimates.

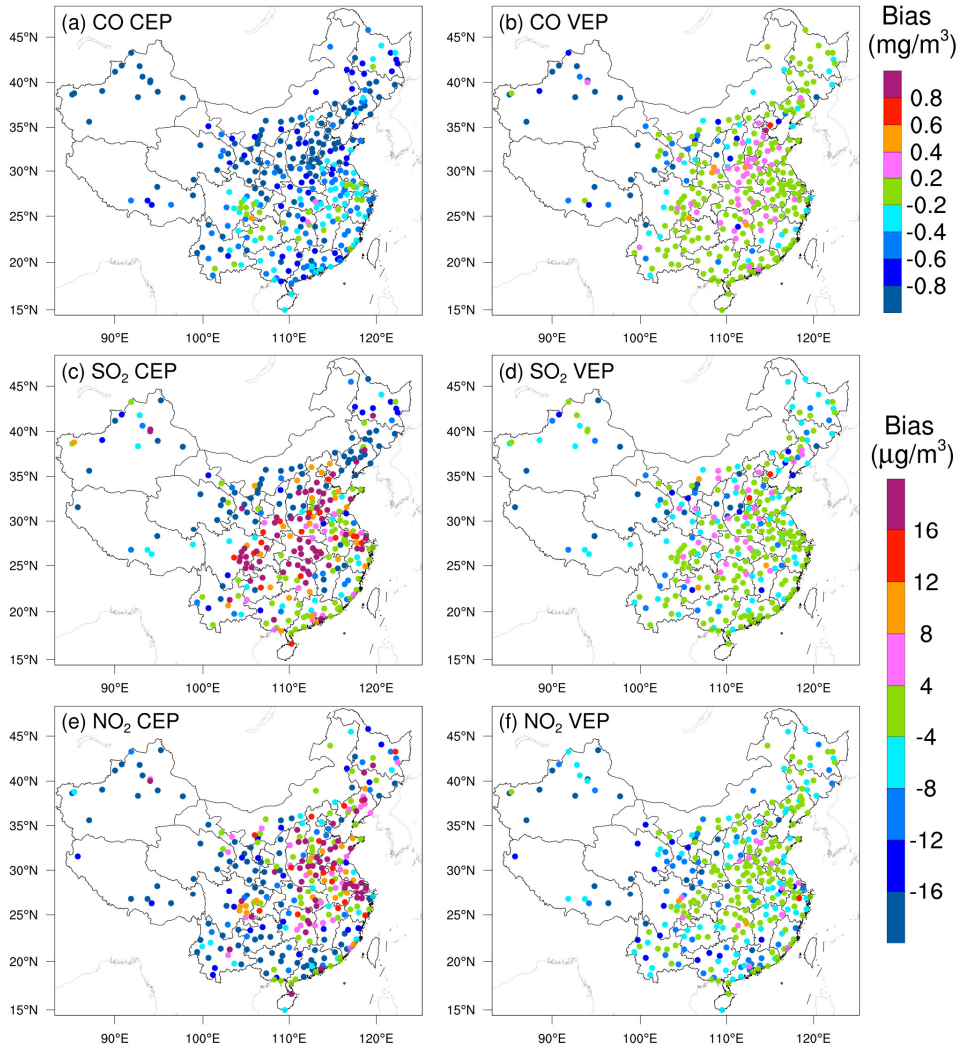

668

669 **Figure 5**. Spatial distribution of the BIAS of the simulated (a, b) CO, (c, d) SO_2 and (e,
670 f) NO_2 with prior (left, CEP) and posterior (right, VEP) emissions. CO unit: mg m^{-3};
671 SO_2 and NO_2 units: μg m^{-3}.

672 Figure 6 shows the spatial distributions of the mean biases of simulated $PM_{2.5}$ and PMC
673 evaluated against the assimilated observations. Similarly, the CEP simulations do not
674 perform well. There are widespread underestimations across the country, with mean
675 biases of -24.0 and -32.4 μg m^{-3}. After data assimilation, the performance of VEP
676 simulations is significantly improved. The biases decrease by 72.1% and 90.4% to -6.7
677 and -3.1 μg m^{-3}, the RMSEs decrease by 41.2% and 40.7% to 29.6 and 24.6 μg m^{-3}, and
678 the CORRs increase by 35.9% and 176.0% to 0.87 and 0.69 for $PM_{2.5}$ and PMC,
679 respectively. Overall, 89.6% and 97.2% of the assimilation sites are improved for $PM_{2.5}$

and PMC, respectively. However, compared with the results of the 3 gaseous pollutants, there are sites with large biases scattered throughout the whole domain. Besides the potential overadjusted or contradictory adjustments of emissions as in the 3 gas species, It may also be related to the complex precursors and complex homogeneous and heterogeneous chemical reactions and transformation processes of secondary $PM_{2.5}$, and the fact that we do not simulate the time variation of dust blowing caused by wind speed for PMC due to the lack of land cover data that is compatible with the CMAQ dust module and agricultural activities data to identify dust source regions.

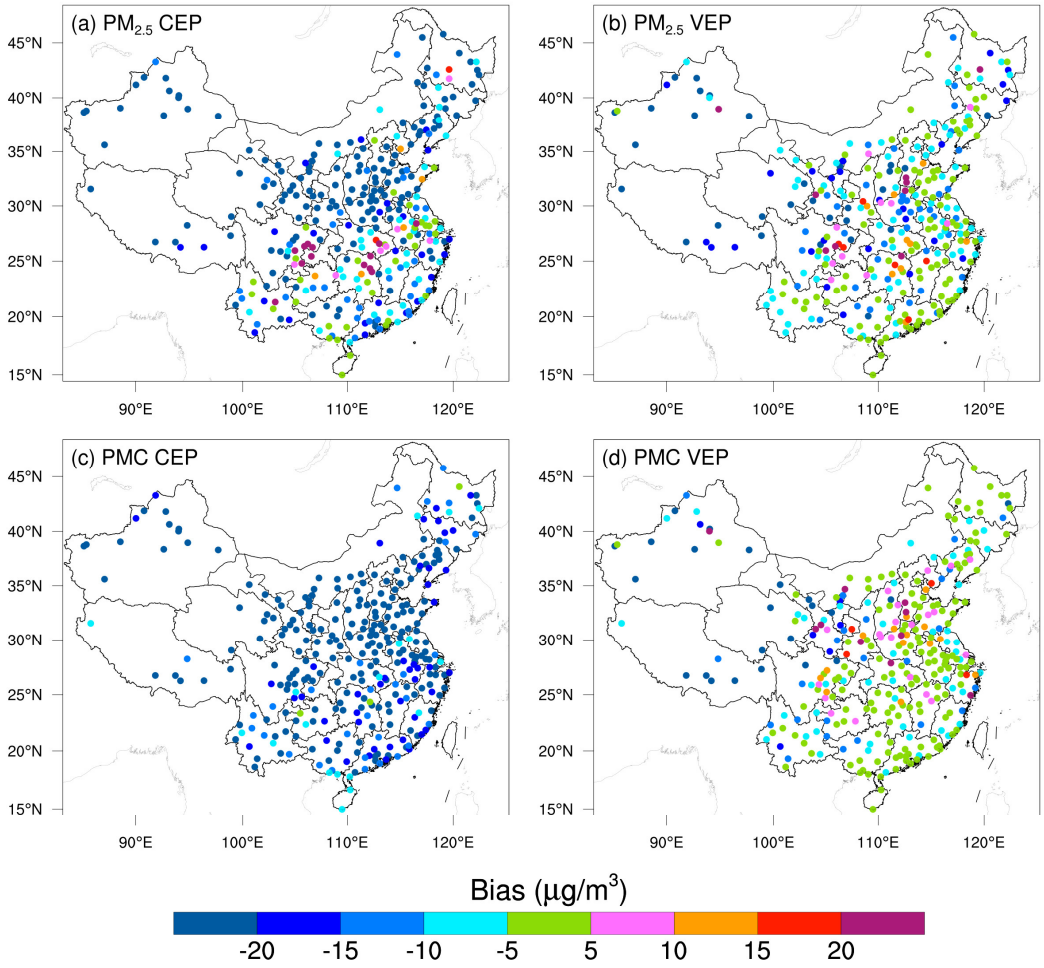

Figure 6. Same as in Figure 5 but for $PM_{2.5}$ and PMC.

Figure 7 and Figure 8 show the spatial distributions of the biases calculated against the independent observations for the 5 species. With posterior emissions, the decreasing

ratios of RMSEs range from 26.7% to 42.0%, and the CORRs increase by 13.7-59.0% to 0.62-0.87. Overall, the biases at the independent sites are similar or slightly worse than those at the assimilated sites, which is reasonable since the closer to the assimilated site the independent sites are, the more constraints of observation information can be obtained, and the improvements in optimized state variables of the model are more significant. For example, generally, the transmission distance of NO_2 is relatively short, and remote cities with small emission correlations to the cities with assimilated observations are relatively less constrained, resulting in only a 26.7% decrease in the RMSE.

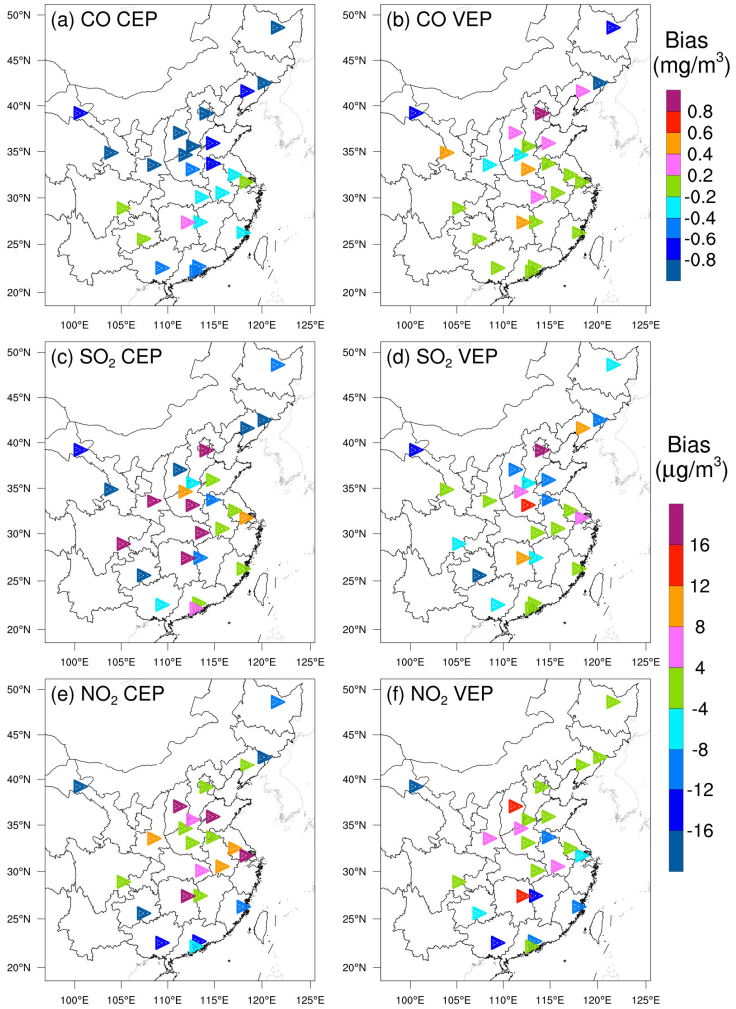

Figure 7. As in Figure 5 but for the independent validation.

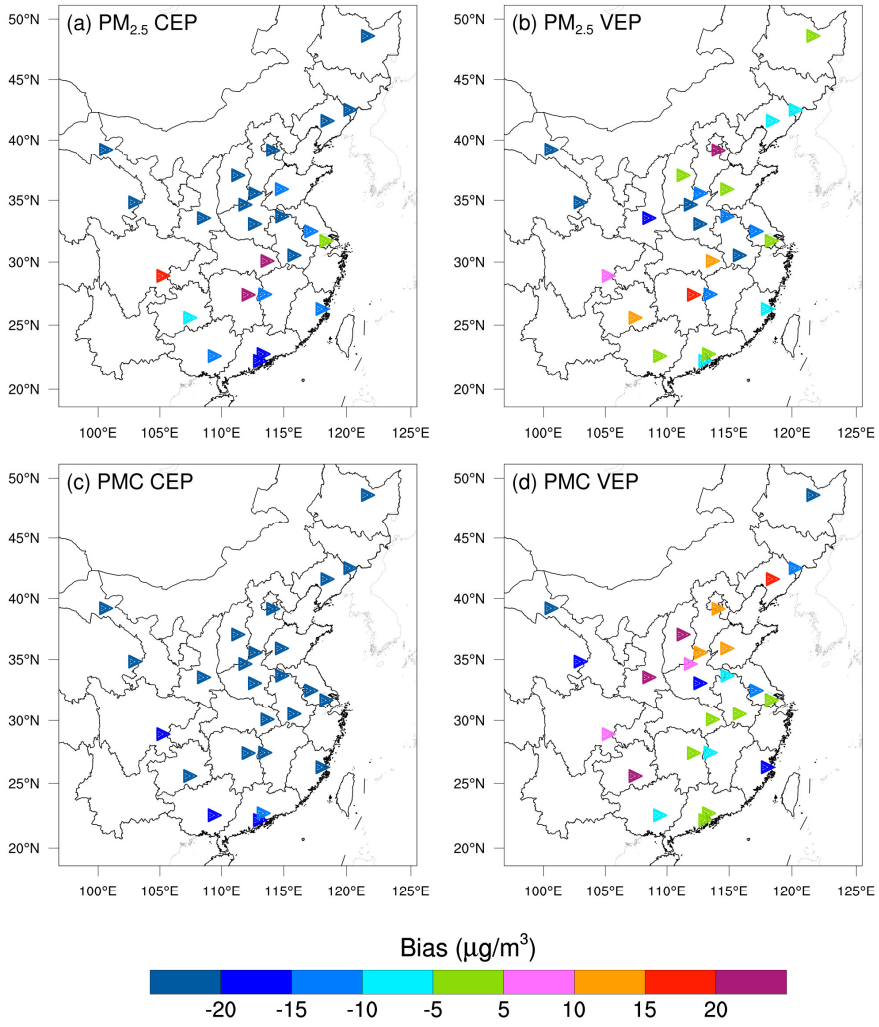

703

704 **Figure 8**. As in Figure 6 but for the independent validation.

705 Compared with the previous studies, Tang et al. (2013) conducted inversion of CO
706 emissions over Beijing and the surrounding areas, the improvements (Table 6) in the
707 RMSE (37-48% vs. 30-51%) and the CORR (both studies ~ 0.81) are comparable, but
708 the biases here could decrease by 90-97%, which is much greater than their 48-64%
709 reductions. Additionally, Chen et al. (2019) showed that the RMSE of simulated SO_2
710 with updated SO_2 emissions decreased by 4.2-52.2% for different regions, and the
711 CORR only increased to 0.69 at most. The improvement is relatively smaller than our
712 results, which may be due to the insufficient adjustment of emissions caused by the
713 underestimated ensemble spread through the inflation method. The better performance
714 in this study may be related to our inversion process that makes the optimized emissions

of the current DA window propagate to the next DA window for further correction.

Table 6. Statistics comparing the pollution concentrations from the simulations with prior (CEP) and posterior (VEP) emissions against assimilated and independent observations, respectively. CO unit: mg m^{-3}; others units: μg m^{-3}.

Species	Mean Obs.	Mean Sim.		BIAS		RMSE		CORR	
		CEP	VEP	CEP	VEP	CEP	VEP	CEP	VEP
Against assimilated observations									
CO	1.43	0.66	1.36	-0.77	-0.08	1.08	0.56	0.46	0.81
SO_2	32.5	34.4	28.4	1.9	-4.1	42.4	17.7	0.39	0.88
NO_2	43.8	40.8	39.0	-2.9	-4.8	25.0	12.3	0.65	0.88
$PM_{2.5}$	77.0	53.1	70.3	-24.0	-6.7	50.3	29.6	0.64	0.87
PMC	40.5	8.1	37.5	-32.4	-3.1	41.5	24.6	0.25	0.69
Against independent observations									
CO	1.54	0.79	1.52	-0.75	-0.02	1.15	0.72	0.59	0.82
SO_2	40.6	39.2	37.3	-1.3	-3.2	44.3	27.2	0.57	0.87
NO_2	50.2	50.0	47.5	-0.3	-2.7	21.7	15.9	0.73	0.83
$PM_{2.5}$	91.5	64.6	84.1	-26.9	-7.4	64.1	37.2	0.62	0.87
PMC	42.0	9.2	40.4	-32.8	-1.6	39.3	26.6	0.39	0.62

* BIAS, mean bias; RMSE, root mean square error; CORR, correlation coefficient

4.1.4 Uncertainty reduction

The uncertainty reduction rate (UR) is another important quantity to evaluate the performance of RAPAS and the effectiveness of in-situ observations in this system (Chevallier et al., 2007; Jiang et al., 2021; Takagi et al., 2011). Following Jiang et al. (2021), the UR is calculated as

$$UR = (1 - \frac{\sigma_{posterior}}{\sigma_{prior}}) \times 100 \quad (19)$$

where $\sigma_{posterior}$ and σ_{prior} are the posterior and prior uncertainties, respectively, which were calculated using the standard deviations of the prior and posterior perturbations (Text S3). Figure 9 shows the URs averaged in each province and the whole mainland China. The URs vary with species, and among the 5 species of emissions, the uncertainties of the $PPM_{2.5}$ and PMC are greatly reduced, while the UR of NO_x emission is lowest, that is because the URs are closely related to the magnitude

settings of prior uncertainties (Jiang et al., 2021). For the whole mainland China, the uncertainties are reduced by 44.4%, 45.0%, 34.3%, 51.8% and 56.1% for CO, SO_2, NO_x, $PPM_{2.5}$ and PMC, respectively. For one species, it also varies across provinces. The URs are usually related to observation coverage, which means that the more observation constraints there are, the more the URs decrease. Additionally, the URs may also relate to emission distributions. Generally, the URs are more significant in the provinces where the observations and emissions are both relatively concentrated (e.g., Tibet), while they are much lower in where the emissions are scattered or relatively uniform, but the observations are only in large cities, even though there are many more observations than other provinces.

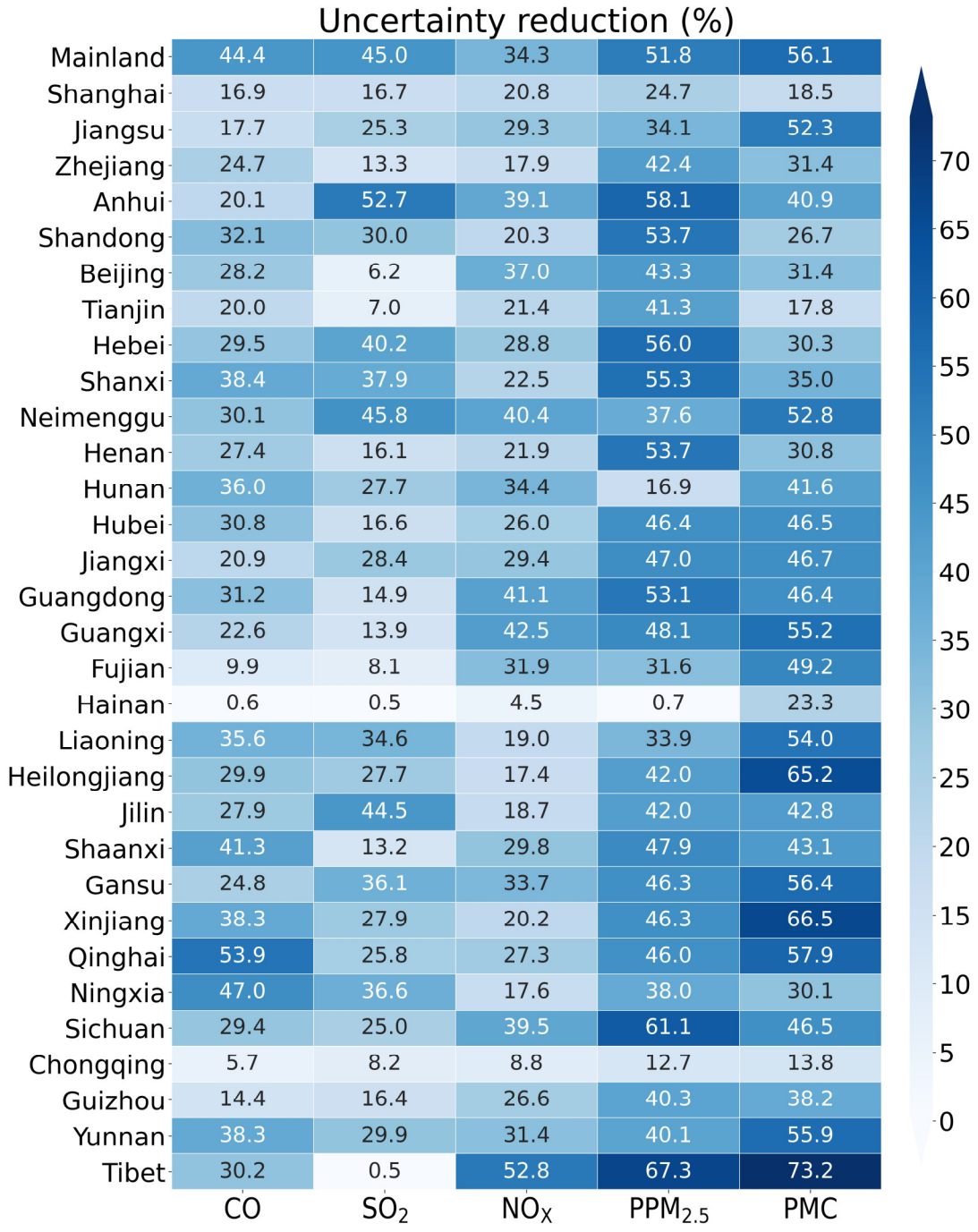

Figure 9. Time-averaged posterior emission uncertainty reduction (%) indicated by the standard deviation reduction of total emissions per province calculated by prior and posterior ensembles.

4.1.5 Evaluation using chi-squared statistics

To diagnose the performance of the EnKF analysis, the chi-squared (χ^2) statistics was calculated, which is generally used to test whether the prior ensemble mean RMSE with

749 respect to the observations is consistent with the prior "total spread" (square root of the
750 sum of ensemble variance and observation error variance). Following Zhang et al.
751 (2015), for the *t*th window, χ^2 is defined as

752 $$\chi_t^2 = (\boldsymbol{y} - \boldsymbol{H}\overline{\boldsymbol{X^b}})^T(\boldsymbol{H}\boldsymbol{P^b}\boldsymbol{H}^T + \boldsymbol{R})^{-1}(\boldsymbol{y} - \boldsymbol{H}\overline{\boldsymbol{X^b}}) \quad (20)$$

753 Figure 10 shows the time series of the relative changes between the prior and posterior
754 emissions and the χ^2 statistics. There are relatively large adjustments of emissions in
755 the first three windows, especially for PMC. After that, the optimality of the five species
756 reaches a more optimal state with successive emission inversion cycle. The χ^2 statistics
757 shows a similar variation characteristics with the daily changes in the emissions. The
758 χ^2 value is slightly greater than 1, indicating that the uncertainties from error covariance
759 statistics do not fully account for the error in the ensemble simulations. A similar
760 situation also appeared in Chen et al. (2019). Further investigations should be
761 conducted to generate larger spreads by accounting for the influence of model errors.
762 Since we imposed a same uncertainty of prior emission at each DA window to partially
763 compensate for the influence of model errors, χ^2 statistics showed small fluctuations,
764 indicating that the system updates emissions consistently and stably.

765

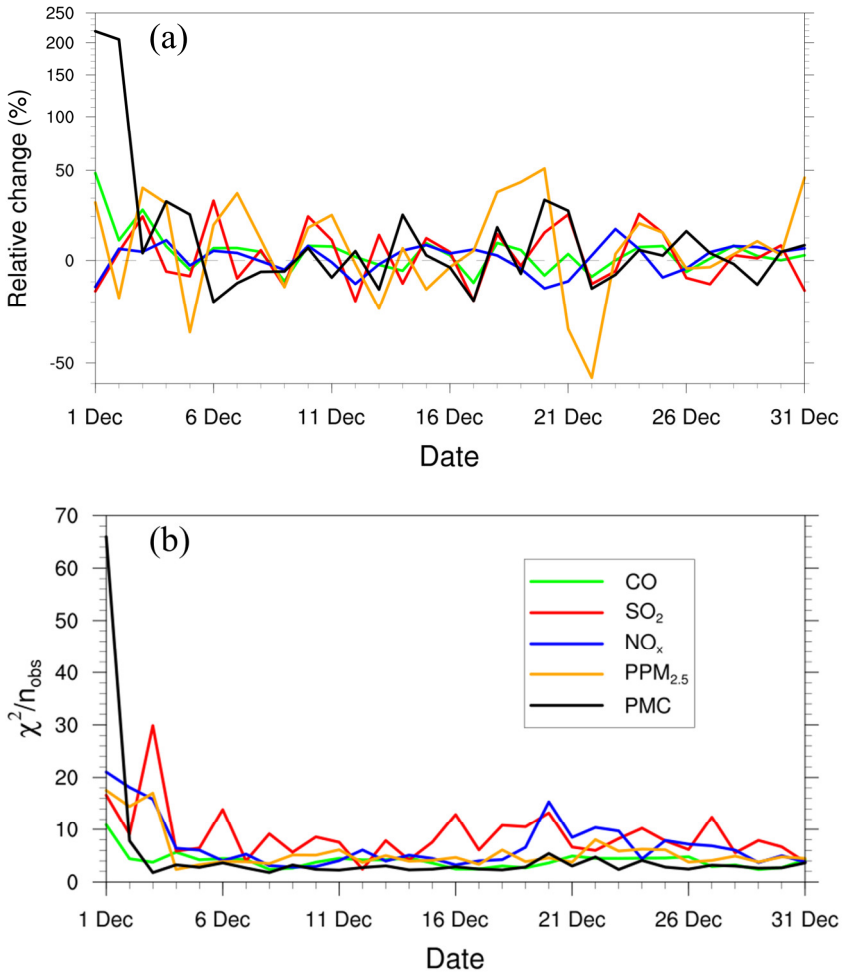

766

767 **Figure 10**. Relative changes (a) in a posteriori emission estimates of CO, SO_2, NO_x,
768 $PPM_{2.5}$ and PMC, and χ^2 statistics (b) of these state vectors in each window.

769 **4.1.6 Evaluation using OSSE**

770 Figure 11 shows the spatial distribution of the error reduction in the posterior emissions
771 of the five species. It can be found that after inversion, in most areas, the emission errors
772 can be reduced by more than 80%, especially in the central and eastern regions with
773 dense observation sites, while in remote areas far away from cities, due to the sparse
774 observation sites, the emission errors are still not well adjusted. Overall, the error
775 reduction rates of CO, SO_2, NO_x, PPM2.5, and PMC are 78.4%, 86.1%, 78.8%, 77.6%,
776 and 72.0%, respectively, indicating that with the ground in-situ observations in China,
777 RAPAS can significantly reduce emission errors, thus has good performance in
778 emission estimates.

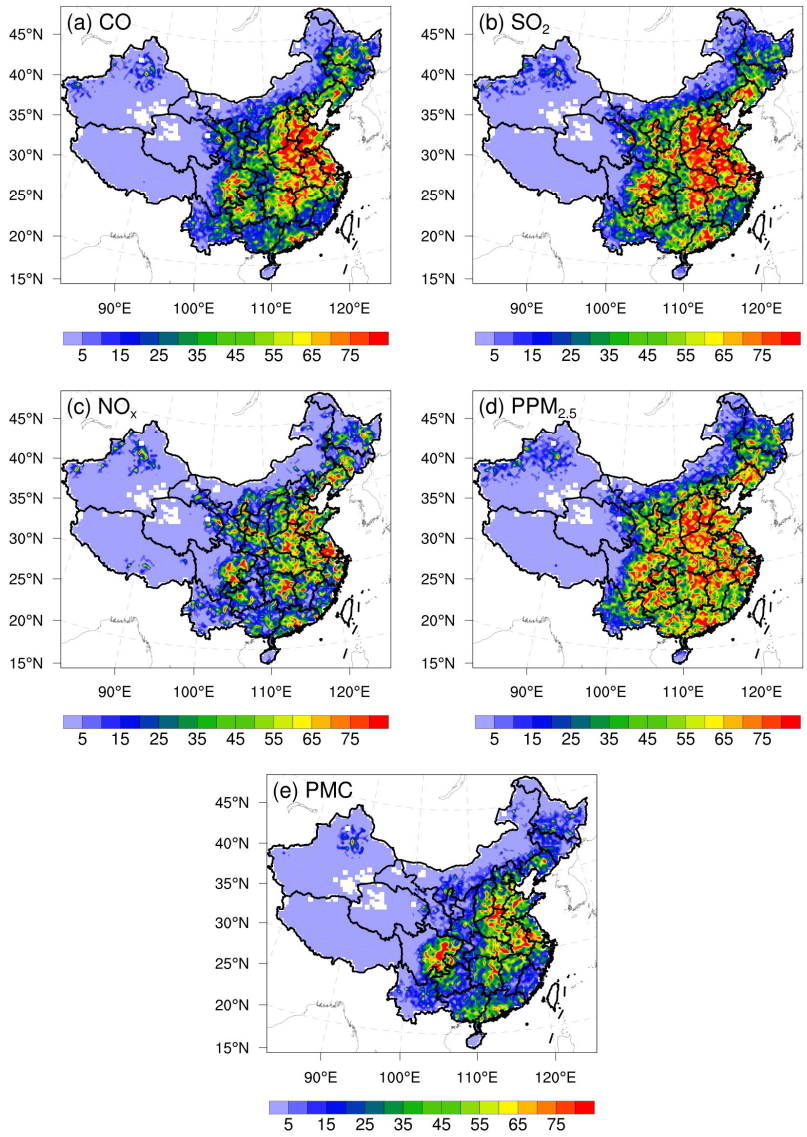

779

780 **Figure 11** Spatial distribution of the error reduction (%) of posterior emissions in the
781 OSSE.

782 **4.2 Inverted emissions**

783 Figure 12 shows the spatial distribution of the temporal averaged prior and posterior
784 emissions and their differences of the emissions in December 2016. It should be noted
785 that the emissions outside China were masked, since the observation sites are all within
786 China in this study, there is little change in the emissions outside China. Higher
787 emissions are mainly concentrated in central and eastern China, especially in the NCP,
788 YRD, and PRD, and lower emissions occur across Northwest and Southern China.

Compared with the prior emissions, posterior CO emissions are considerably increased across most areas of mainland China, especially in northern China, with an overall increase of 129%. Notable underestimation of the prior emissions is also confirmed by previous inversion estimations (Feng et al., 2020b; Tang et al., 2013; Wu et al., 2020) and model evaluations (Kong et al., 2019b). For SO_2, the emission increases mainly occur in Northeast China, Shanxi, Ningxia, Gansu, Fujian, Jiangxi and Yunnan provinces. In SCB, Central China, YRD, and part of NCP, the emissions are significantly reduced. For national total, the SO_2 emission is increased by 20%. For NO_x, although the increment of national total emissions is small, only about 5%, large deviations still exist on regional scale. Obviously, the emissions in the NCP and YRD are reduced, while in the other regions, the emissions of most cities are increased. The changes in $PPM_{2.5}$ emission are similar to SO_2. Compared with the prior emission, the posterior $PPM_{2.5}$ emissions are decreased over central China, SCB and YRD, while the ones in southern and northern China are increased, especially in Shanxi, Shaanxi, Gansu and southern Hebei province. Overall, the relative increase is 95%. For PMC, the posterior emissions are increased over the whole mainland China, with national mean relative increase exceeding 1000%. Larger emission increments mainly occur in the areas where have significant anthropogenic emissions of CO and $PPM_{2.5}$, indicating that the large underestimations of PMC emissions in the prior inventory may be mainly attributed to the underestimations of anthropogenic activities. In addition, the absence of natural dust is another reason, as the wind-blown dust scheme was not applied in this study. Overall, PM10 emissions (PPM2.5+PMC) increased by 318%. If we assume that all the increment in PM_{10} emissions is all from natural dust, that means the contribution of natural dust accounts for 75% of total PM_{10} emissions, which is consistent with the source apportionment of PM_{10} of 75% in Changsha in Central China (Li et al., 2010). Large PMC emission increment are also found in Ma et al (2019).

Detailed estimation of posterior emissions and relative changes compared to prior emissions in each province and the whole mainland China is given in Table S1. The evaluation results for July show that the emission uncertainty can still be significantly

reduced, and the performance of the system in July is comparable to that in December (Table S2). Additionally, the seasonal variation of emissions can be well reflected (Figures S4 and S5), which means that our system can perform well at different times of the year. Note that the differences, excluding PMC, between the prior and posterior emissions mainly reflect the deficiencies of the prior emissions because the times of the prior emissions and the observations are completely consistent in this study.

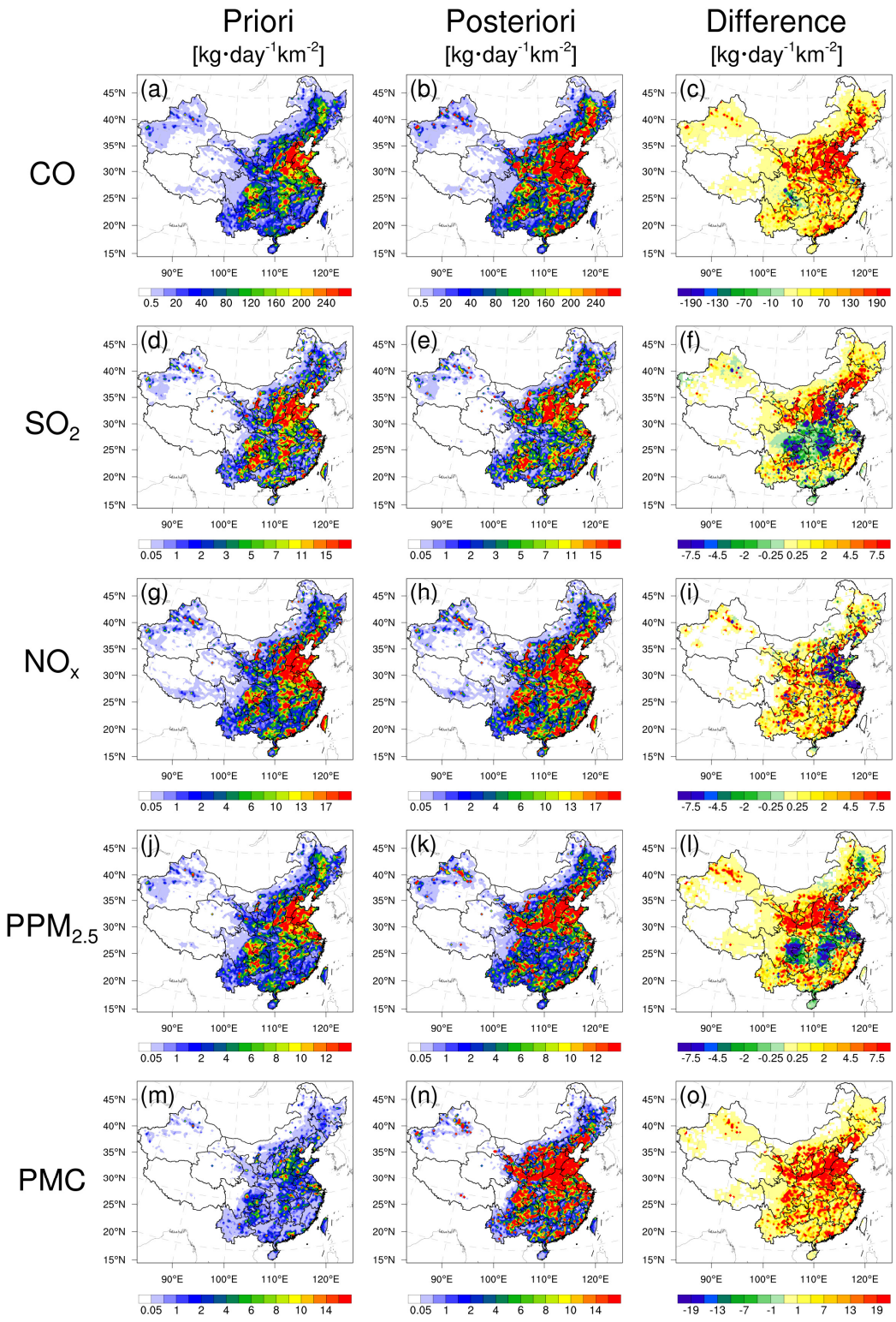

824

825 **Figure 12**. Spatial distribution of the time-averaged prior emissions (left column, MEIC
826 2016), posterior emissions (middle column), and differences (right column, posterior
827 minus prior).

4.3 Sensitivity tests

4.3.1 Impact of prior inventories

Various prior inventories have great differences in space allocation and emission magnitude. Inversion results can be sensitive to a priori emissions if the observation is insufficient (Gurney et al., 2004; He et al., 2018). MEIC 2012 is used as an alternative a priori in EMS2 to investigate the impact of different prior emissions on the posteriori. Figure 13 shows the time series of the relative differences in daily posterior emissions of the five species between the EMDA (base) and EMS2 experiments. Overall, the differences between the two posterior emissions gradually decrease over time. At the beginning, the differences in the CO, SO_2, NO_x, $PPM_{2.5}$ and PMC between the two inventories (i.e., MEIC 2012 vs MEIC 2016) are 17.5%, 114.5%, 30.8%, 46.0% and 72.0%, respectively, while during the last ten days, the differences of the two posterior emissions have decreased to 2.5%, 4.5%, 4.5%, -8.9% and 3.0%, respectively. In addition, it also could be found that the species that has larger emission differences at the beginning take a longer time (namely more DA steps) to achieve convergence. The quick convergence of PMC emission is attributed to the large prior uncertainty of 100% used in the first 3 DA windows. Different from the other species, there are significant negative deviations of $PPM_{2.5}$ emissions between the two experiments. That may be due to the positive deviations in the precursors of $PM_{2.5}$ (i.e., SO_2 and NO_x), which will lead to a larger amount of secondary production. To balance the total $PM_{2.5}$ concentration, the $PPM_{2.5}$ emissions will be reduced. We compare the $PM_{2.5}$ concentrations simulated by the two optimized inventories and find that they are almost the same (Figure S6). Overall, this indicates that the observation in China is sufficient in inferring the emissions, and our system is rather robust. Meanwhile, it also suggests that the monthly posterior emissions shown in Sect. 4.2 are still underestimated to a certain extent.

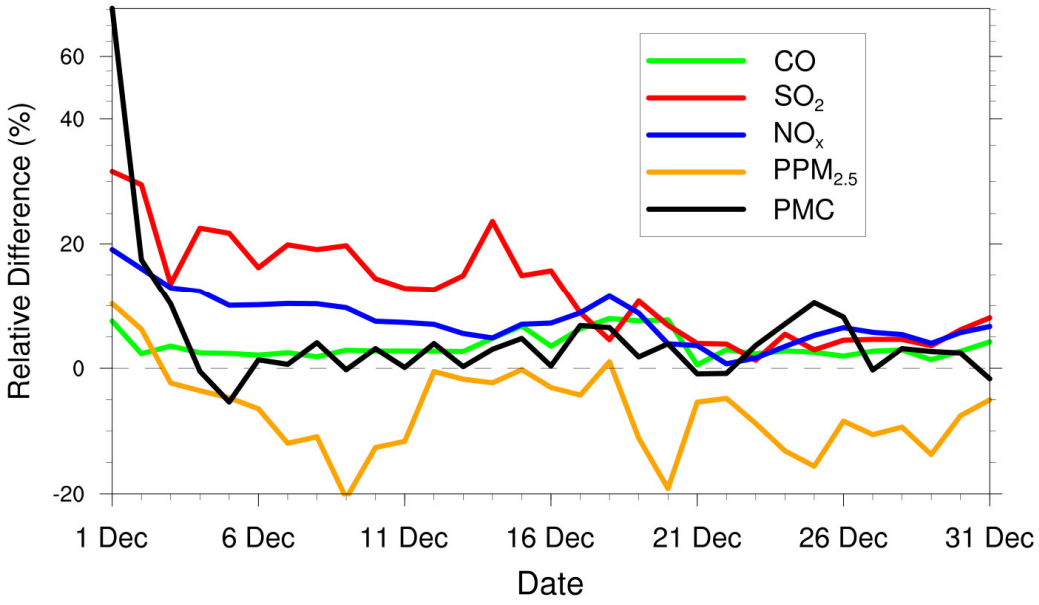

854

855 **Figure 13**. Relative differences in CO, SO_2, NO_x, $PPM_{2.5}$ and PMC emissions (%, the
856 ratio of absolute difference to EMDA) between the EMDA and EMS2 experiments.
857

858 **4.3.2 Impact of prior uncertainties settings**

859 The uncertainty of prior emissions determines how closely the analysis is weighted
860 toward the background and observation, but information about prior uncertainties is
861 generally not readily available. To evaluate the possible influence of prior uncertainties
862 on the optimized emissions, we increased/reduced the uncertainties after 3 days of
863 cycling, namely starting at 0000 UTC, 3 December, by 25% and 50 % in EMS3 (-50%),
864 EMS4 (-25%), EMS5 (+25%) and EMS6 (+50%), respectively. Table 7 summarizes the
865 emission changes with different prior uncertainties settings in EMS3-6 experiments. To
866 better understand the response of the system to the emission uncertainty settings, Figure
867 14 shows the time series of SO_2 emission changes, the Chi-square statistics and the
868 RMSEs of simulated SO_2 with emissions updated in the EMDA and EMS3-6
869 experiments over the YRD and NCP (Figure 2). Compared with the EMDA, when the
870 uncertainties are decreased (increased), the emissions of the 5 species decrease
871 (increase) accordingly. That is because the posterior emissions of the 5 species are
872 larger than the prior emissions, and as shown in Figure 14a-d, larger uncertainty will

lead to a faster convergence, resulting in larger posterior emissions. It also could be found from Figure 14 that a faster convergence will indeed reduce the RMSE of the simulated concentration with the posterior emissions in the early stage of the experiment, but in the later stage of the experiment, there are no significant differences for the RMSE and Chi-square statistics among the different experiments. However, the day-to-day changes in emissions can also cause slight fluctuations. In addition, it shows that when greater uncertainties are set, the day-to-day changes in emissions are also more drastic, resulting in a larger RMSE as shown in NCP. Moreover, those significant day-to-day variations of estimated emissions may not be in line with the actual situation. Due to the spatial-temporal inhomogeneity of emissions, the differences of Chi-square statistics between the YRD and NCP show that it may be necessary to apply different a priori uncertainties according to different regions (Chen et al., 2019). Therefore, when using an EnKF system for emission estimation, we have to be very careful about the setting of these errors. Overall, the uncertainties chosen in EMDA aim to minimize the deviation of the concentration fields and maintain the stability of inversion.

Table 7. Relative differences in CO, SO_2, NO_x, $PPM_{2.5}$ and PMC emissions (%, the ratio of absolute difference to EMDA) between the EMDA and EMS3-6 experiments.

Species	EMS3	EMS4	EMS5	EMS6
CO	-8.6	-4	3	5.2
SO_2	-14	-5.7	3.6	6.8
NO_x	-6.5	-3	2.8	4.5
$PPM_{2.5}$	-16.5	-7.8	4.6	8.7
PMC	-18.5	-8.2	7.3	13.1

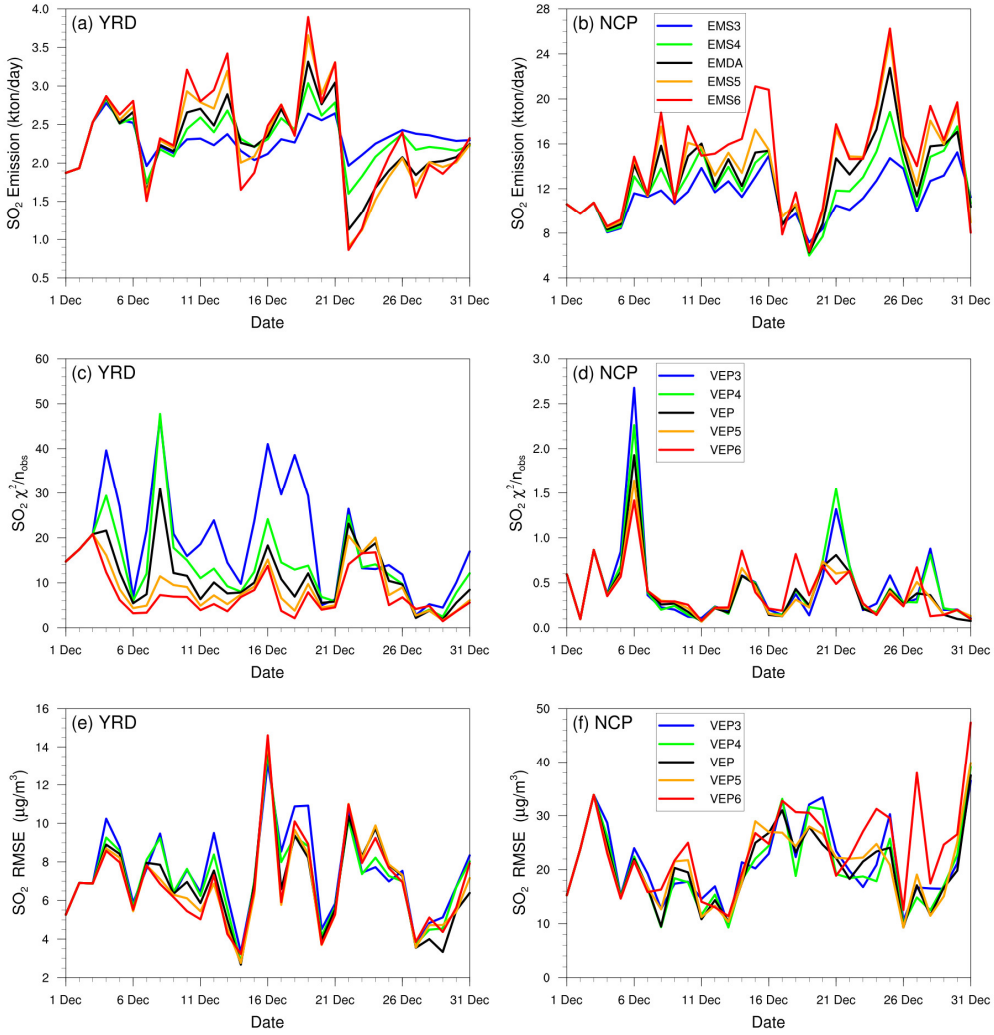

Figure 14. Time-series of SO_2 emission changes, the Chi-square statistics and the RMSE of simulated SO_2 with updated SO_2 emissions in the EMDA and EMS3-6 experiments over the Yangtze River Delta (YRD) and North China Plain (NCP).

4.3.3 Impact of observation error settings

Another factor that determines the relative weights of the observation and background in the analysis is observation errors. A proper estimate of the observation error is also important in regard to the filter performance, but observation errors are not provided with the dataset. The observation error is usually set to a fixed value (Ma et al., 2019), a specific proportion of the observation value (Tang et al., 2013) or the value calculated by combining measurement error with representative error as used in this study. Generally, the performance of the data assimilation is quite sensitive to the specification

of observation error (Tang et al., 2013). To evaluate the influence of observation error on the optimized emissions, a sensitivity experiment (EMS7) with doubled observation error was conducted. Overall, the spatial distribution of emissions after optimization is almost the same as that of the EMDA experiment, but the increment is lower (Figure S7), resulting in a weaker estimate of the national total emission for each species. That is because that the observation error becomes large, the system will be more convinced of the prior emission and reduce the effect of observation information. Figure 15 shows the time series of simulated and observed daily concentrations and their RMSEs verified against the assimilated sites. The simulations in VEP7 usually perform worse, with larger biases and RMSEs than those of VEP (Figures S8 and S9), especially in most of western and southern China where posterior emissions are still significantly underestimated. These results usually correspond to sluggish emission changes and large Chi-square statistics (Figure S10), suggesting that too large observation error may substantially impact the estimated emissions.

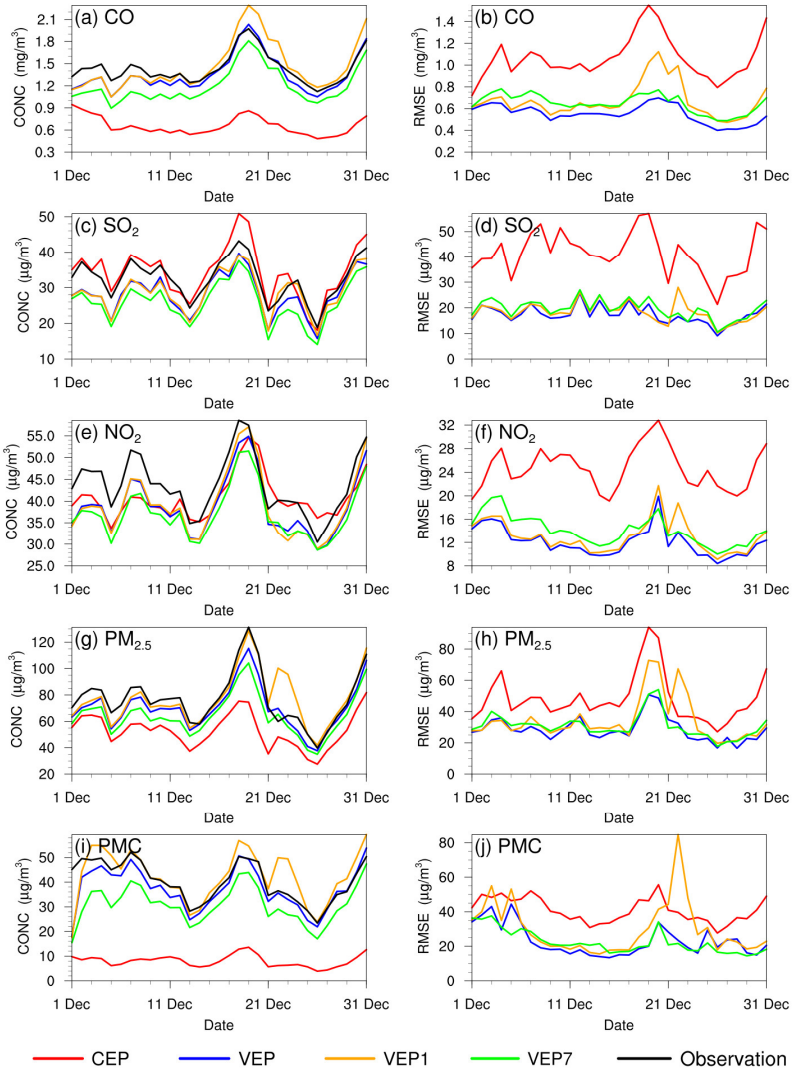

Figure 15. Time series of the daily concentrations (CONC, left) and root mean square error (RMSE, right) obtained from CEP, VEP, VEP1, and VEP7. The simulations were verified against the assimilated sites.

4.3.4 Impact of the IC optimization of the first window

Many studies have shown that there would be large emission discrepancies resulting from the IC errors (Jiang et al., 2013a; Miyazaki et al., 2017; Tang et al., 2013), which means that if the IC is not optimized, the errors of concentrations would be compensated through the adjustment of emissions. To evaluate the impact of the IC optimization of the first window on the emission inversions, the EMS8 experiment without the IA step was conducted. Figure 16 shows the time series of the relative differences in daily

posterior emissions of the five species between the EMDA and EMS8 experiments. It can be found that the optimization of IC has great impact on the emission inversions of long-lived species (i.e., CO). The overall difference in the inverted CO emissions between the two experiments is about 5.3%, and in the first few windows, the maximum difference can reach 26.1%. For the short-lived species, the IC optimization has little impact on the emission, for example, the averaged emission differences of SO_2, NO_x and PMC in the two experiments are 0.3%, 0.3% and 0.9%, respectively. For PPM2.5, it is affected not only by the primary emission, but also by the complex chemistry of its precursors. Therefore, the difference between the two experiments fluctuates at a certain extent, with overall difference of 2%. It is worth noting that with the gradual disappearance of the benefit of IC assimilation, the two experiments can reach a unified state after some windows. For CO, the impact of IA on emission inversion lasts about half a month. These results indicate that removing the bias of IC of the first DA window is essential for subsequent inverse analysis (Jiang et al., 2017).

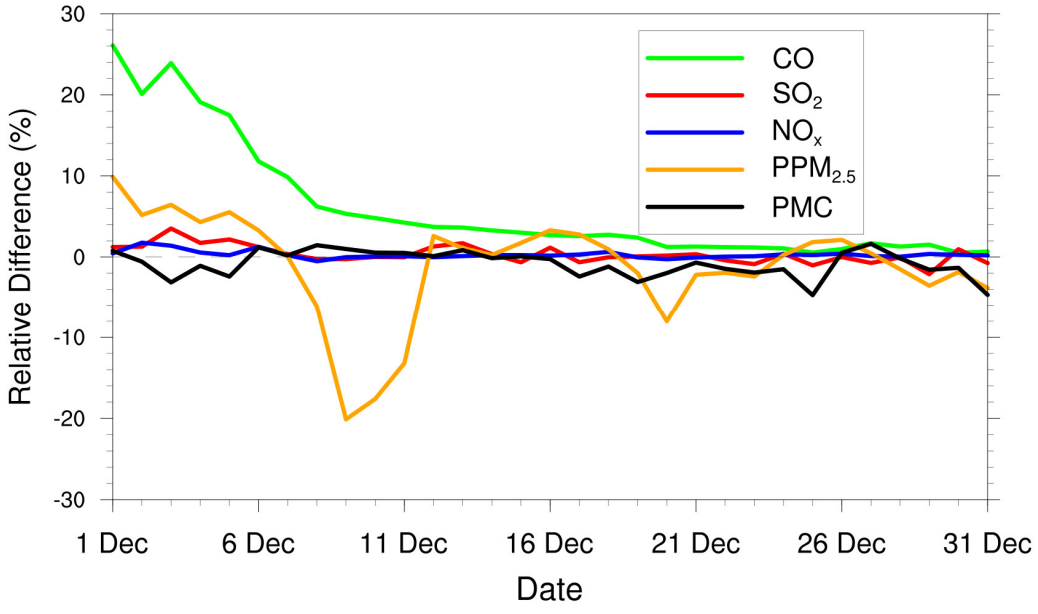

Figure 16. Relative differences in CO, SO2, NOx, PPM2.5 and PMC emissions (%, the ratio of absolute difference to EMDA) between the EMDA and EMS8.

4.3.5 The advantages of "two-step" scheme

Adjusting the ICs and emissions simultaneously (i.e., "one-step" scheme) has been applied to constrain prior emissions in many previous studies (Evensen, 2009; Kong et al., 2019a). To investigate the impact of different methods on the optimized emissions, a sensitivity test (EMS1) was performed, in which the initial fields of each DA window were optimized using the 3DVAR algorithm directly. Compared with our "two-step" method (EMDA), the posterior emissions of EMS1 are increased by 7%, 1.4%, 0.6%, 22.2%, and 17.2% for CO, SO_2, NO_x, $PM_{2.5}$ and PMC, respectively. Overall, there is no significant difference between the two methods for NOx and SO2, but for CO, it can be clearly seen that the difference increases with the inversion (Figure S11). As mentioned previously, in the "two-step" scheme, the unresolved posterior emission error will be fed back to the initial field of the next window through sufficient mixed simulation within one day for timely optimization. Meanwhile, the system always maintains the mass balance of pollutants. In this way, the system updates emissions more consistently and stably. If the emission in one window is overestimated, in this way, it could be compensated in the next window with lower estimates. In contrast, when initial fields assimilating with observations simultaneously at each window, the overestimation will not be corrected and will accumulate to the end. We also evaluate the posterior emissions of EMS1 using the same method as shown in Sect. 4.1.3. Overall, compared to the base experiment (EMDA), the performance of EMS1 is significantly worse, with RMSEs of CO, SO_2, NO_2, $PM_{2.5}$ and PMC increasing from 0.56 mg m^{-3}, 17.7, 12.3, 29.6, and 24.6 μg m^{-3} to 0.69 mg m^{-3}, 18.8, 13.3, 36.8, and 33.3 μg m^{-3}, respectively (Figure 15). Additionally, it can be seen from the figure that the results of the two experiments are relatively close at the beginning and during the heavy pollution period (16-21 December). However, after that, the simulated results with "one-step" inversion emissions are significantly higher than the observations, and these large biases continue until the end. The results verified against the independent sites also show a similar situation (Figure S8). The reason may be that during the period of heavy pollution, the WRF-CMAQ (off-line model) does not consider the feedback process of meteorology

and chemistry, resulting in low simulations. Therefore, the system will compensate for the underestimated concentrations caused by the model error through more emissions, resulting in the overestimation of emissions. The accumulation of emission error in each independent window further leads to the overestimation of concentration after the end of high pollution, especially for species with a long lifetime (e.g., CO). On the contrary, this overestimation will be corrected quickly in the subsequent inversion using the "two-step" inversion scheme in this study (Figure S11), so as to ensure the stability of the system. Additionally, the other "one-step" experiment, taking MEIC 2012 as prior emissions, was conducted. However, the relative differences (Figure S12) in posterior emissions between this experiment and the EMS1 did not converge like that between EMDA and EMS2 with "two-step" scheme (Figure 13), which further demonstrates the advantages of the "two-step" scheme. It should be noted that the model performance depends on many factors but does not affect the advantage of the "two-step" scheme.

4.4 Discussion

Optimal state estimation using an EnKF relies on the assumption of unbiased Gaussian prior error, which is not guaranteed in such highly nonlinear and large biases systems In this study, some pollutants (e.g., CO, PMC) have very large simulated biases, thus if a small uncertainty is adopted, the emission bias cannot been fully reduced, while if a very large uncertainty is adopted, then the degree of freedom of adjustment is too large, and the inverted daily emissions will fluctuate abnormally. Therefore, we only set a larger prior uncertainty in the first three windows, adopted a moderate uncertainty in the following windows, and used a "two-step" inversion scheme and cyclic iteration to gradually correct the emission errors. Figure 10(a) shows the time series of the relative differences between the prior and posterior emissions in each window. There are the relatively large adjustments for the emissions in the first three windows, especially for PMC, but the adjustment ranges of the five species after the first 3 windows are basically within the uncertainty range (e.g., ±25%), indicating that with this scheme, the EnKF method used in this system still has a good performance in emission inversion.

The model-data mismatch error not only comes from the emissions, but also from the inherent model errors arising from model structure, discretization, parameterizations and the biases in the simulated meteorological fields. Neglecting model errors would attribute all uncertainties to emissions, and lead to considerable biases in the estimated emissions. In the version of CMAQ model used in this study, there is no heterogeneous reactions (Quan et al., 2015; Wang et al., 2017), the parameterization scheme for the formation of secondary organic aerosol (SOA) is imperfect (Carlton et al., 2008; Jiang et al., 2012; Yang et al., 2019), no feedback between chemistry and meteorology is considered, and we used an idea profile for chemical lateral boundary conditions. All of the above problems can lead to underestimated concentrations of pollutants, which in turn require more emissions to compensate, leading to overestimations in emissions. In addition, previous studies have shown that the emission of ammonia in the MEIC inventory was underestimated (Kong et al., 2019b; Paulot et al., 2014; Zhang et al., 2018). Due to lack of ammonia observations, our system does not include emission estimates of ammonia, which means that the concentration of ammonium aerosol was underestimated in this system, also resulting in an overestimation in the $PPM_{2.5}$ emission. Wind-blown dust was also not simulated here, thus the PMC emission inverted in this system do not only come from anthropogenic activities, but also from natural sources. Although some of these shortcomings could be solved in the future by updating the CTM model, there will still be errors in each parameterization and each process. Generally, parameter estimation method was used to reduce the model errors, in which, some uncertain parameters were included in the augmented state vector and were optimized synchronously based on the available observations (Brandhorst et al., 2017; Evensen, 2009). However, it is still quite difficult to identify the key uncertain parameters of different species in different models, which generally comes not only from the complex atmospheric chemical model, but also from hundreds of model inputs (Tang et al., 2013). Another method is bias correction, which treats the model error as a bias term, and includes it in the augmented state vector (Brandhorst et al., 2017; De Lannoy et al., 2007; Keppenne et al., 2005). In addition, the weak-constraint 4D-Var

method can also be used to reduce the model errors, which adds a correction term in the model integration to account for the different sources of model error (Sasaki, 1970). Although reliable diagnosis of model error is still a challenge at present (Laloyaux et al., 2020), it should be considered in an assimilation system. We will consider model errors in our system in the future to obtain better emission estimates.

Independent variable localization was adopted to avoid potential spurious correlations across different species in this study. However, the transmission scales for different species in different regions are still different, and a more accurate localization range could be obtained through backward trajectory analysis. Although Hamer et al. (2015) successfully used O_3 observations to estimate NOx and VOC emissions within the 4D-var framework within an idealised model, O_3 observations are not assimilated to improve NO_x and VOC emissions using cross-species information due to the strong nonlinear effects within the O_3-NO_x-VOC relationship (Wang et al., 2019b), in which the O_3 concentration and NO_x (VOC) emissions are positively correlated in the NO_x (VOC)-limited region and negatively correlated in the VOC (NO_x)-limited region (Tang et al., 2011). This work will be followed up by an ongoing work using available VOC observations. The optimization of the initial fields or emissions of NO_2 may also change the O_3-NO_x-VOC relationship. Assuming that NO_2 is underestimated, the NO_2 concentration increases after assimilation, but the VOC concentration remains unchanged, then in the NOx (VOC)-limited region, the subsequent generation of O_3 will increase (decrease); Conversely, the ozone concentration errors caused by assimilating NO_2 will also affect the subsequent NOx emission inversion. Similarly, the model may not be able to resolve local-scale NO_2 well because of uniform distribution of concentration over the whole grid. Therefore, the model is shifted towards a NO_x (VOC)-limited regime in high (low) pollution regions, which negatively impacts results by perturbing ozone chemistry in unrealistic ways (Inness et al., 2015). To evaluate the influence of O_3-NO_x-VOC relationship change and model resolution on inversion, we also further conducted a nested emission inversion on a densely observed area (the Yangtze River Delta, China) with a grid spacing of 12 km (Feng et al., 2022). The study

period is the same as this study. Results showed that the NOx emissions in the Yangtze River Delta retrieved at two resolutions are almost the same (14.7 kt/day vs. 13.4 kt/day), with a difference of 8.8%, indicating that the emissions can be adjusted effectively by RAPAS. As shown previously, the concentrations after DA are obviously underestimated in western China, indicating that the inverted emissions over these regions still have large uncertainties because of the sparsity of observations that are spatially insufficient for sampling the inhomogeneity of emissions. Therefore, further investigations with joint assimilation of multisource observations (e.g., satellite) are also underway.

When comparing the performances of the “two-step” and “one-step” schemes, for the “one-step” scheme, we use a combination assimilation method, namely 3DVAR for the optimizations of initial fields and EnKF for emission inversions in each DA window, which is similar as Jiang et al., (2017), but different from most previous studies (Miyazaki et al., 2017; Tang et al., 2013). Because most previous “one-step” assimilation studies used only one method (i.e., EnKF). This combination method may cause the comparison less than perfect. However, it should be noted that, even using the same method (such as EnKF) to optimize the emission of the current window and the initial field of the next window simultaneously (Peng et al., 2018), the initial field estimation errors will still be mixed in the simulated concentration field, resulting in unreasonable emission compensation in the next window. In “one-step” scheme, the essence is to build a good initial field in the high levels. Schwartz et al. (2014) compared the performances of EnKF and 3DVAR in optimizing initial fields, and found that 3DVAR method can obtain a better initial field than EnKF method. Therefore, we believe that in this comparison, a combinatorial assimilation approach used in the "one-step" scheme is an acceptable approach, and the conclusion is credible, that the “two-step” scheme has better performances than the “one-step” scheme in emission estimates.

NOx is mainly emitted by transportation (Li et al., 2017), which can better reflect the level of economic activities to a certain extent. Weekly emission changes were also explored to verify the performance of the system in depicting emission changes (Figure

S13). Although the "weekend effect" of emissions in China is not significant (Wang et al., 2014; Wang et al., 2015), the posterior NOx emission changes showed a good agreement with the observations. In our previous studies (Feng et al., 2020a; Feng et al., 2020b), the system was successfully applied to optimize NOx and CO emissions, respectively. The inverted emission changes were also in line with the time points of epidemic control. Additionally, the emission changes can well reflect the emission migration from developed regions or urban areas to developing regions or surrounding areas over recent years, which were consistent with the emission control strategies in China. Although the system does not consider the model error, resulting in a certain difference between the posterior emission and the actual emission, the spatiotemporal changes in posterior emissions are relatively reasonable, which can be used to monitor emission changes and make emission regulations.

5 Summary and conclusions

In this study, we developed a Regional multi-Air Pollutant Assimilation System (RAPASv1.0) based on the WRF/CMAQ model, 3DVAR and EnKF algorithm. RAPAS can quantitatively optimize gridded emissions of CO, SO_2, NO_x, $PPM_{2.5}$ and PMC on regional scale by simultaneously assimilating hourly in-situ measurements of CO, SO_2, NO_2, $PM_{2.5}$ and PM_{10}. This system includes two subsystems, namely the IA subsystem and the EI subsystem, which optimizes the chemical ICs, and infers the anthropogenic emissions, respectively.

Taking the 2016 Multi-resolution Emission Inventory for China (MEIC 2016) in December as a priori, the emissions of CO, SO_2, NO_x, $PPM_{2.5}$ and PMC in December 2016 were inferred through assimilating the corresponding nationwide observations over China. The optimized ICs and posterior emissions were examined against the assimilated and independent observations through parallel forward simulation experiments with and without DA. Sensitivity tests are also performed to investigate the impact of different inversion processes, prior emissions, prior uncertainties and observation errors on the emission estimates.

The results show that RAPAS has a good performance in assimilating ground in-situ observations, with the calculated emission uncertainties reduced by 44.4%, 45.0%, 34.3%, 51.8% and 56.1% for CO, SO_2, NO_x, $PPM_{2.5}$ and PMC, respectively. It can also significantly improve the simulations, the RMSEs of the simulated concentrations with posterior emissions decreased by 40.1-56.3%, and the CORRs increased from 0.26-0.66 to 0.69-0.87 for different species. The OSSE experiment shows that the error of posterior CO, SO_2, NO_x, PPM2.5, and PMC could be reduced by 78.4%, 86.1%, 78.8%, 77.6%, and 72.0%, respectively. Overall, compared with the prior emissions (MEIC 2016), the posterior emissions increased by 129%, 20%, 5% and 95% for CO, SO_2, NO_x and $PPM_{2.5}$, respectively. The posterior PMC emissions, which included anthropogenic and natural dust contributions, increased by 1045%. The sensitivity tests with different inversion processes show that the "two-step" scheme in emission inversion outperforms the joint adjustment of ICs and emissions ("one-step" scheme), especially after heavy pollution. The sensitivity tests with different prior inventories show the observation in China is sufficient in inferring the emissions, and our system is less dependent on prior inventories. Additionally, the sensitivity tests with different prior uncertainties indicate that when the posterior emissions are larger than the prior emissions, the emissions decrease/increase with the decreases/increases of uncertainties because of the different convergence rates. These results demonstrate the advantage of the two-step method in emission inversion in that the inversion errors of the last window could be transferred to the current window for further optimization and the robustness of the emissions estimated from RAPAS using the nationwide observations over China. It should be noted that the system usually responds slowly to too small a priori uncertainty or too large observation error, which may result in large errors in the estimated emissions.

In summary, the comprehensive evaluation and sensitivity tests reveal that RAPAS could serve as a useful tool for accurately quantifying the spatial and temporal changes of multi-species emissions at regional scales and near-real time, which will be helpful for the air pollution control in China, and the other regions around the world with dense ground observation networks.

Code and data availability

The codes of RAPAS v1.0 are available at https://doi.org/10.5281/zenodo.5566225. The WRF model code is open-source code and can be obtained from the WRF Model User's Page (https://www2.mmm.ucar.edu/wrf/users, last access: 25 April 2021). The CMAQ model is available through an open license as well (https://www.epa.gov/cmaq , last access: 25 April 2021). The observation and emission data used in this paper are available at https://doi.org/10.5281/zenodo.4718290 (Feng and Jiang, 2021).

Author contribution

SF, FJ, ZW and ZJ developed RAPAS v1.0. SF and FJ designed the research. SF performed model simulations, analyzed data, and prepared the paper with contributions from all co-authors. FJ supervised the model development project and assisted in conceptualization and writing. HW, WH, YS, LZ, YZ, CL, and WJ contributed to the discussion and improvement of the paper.

Competing interests

The authors declare that they have no conflict of interest.

Acknowledgements

This work is supported by the National Key R&D Program of China (Grant No. 2016YFA0600204), the National Natural Science Foundation of China (Grant No. 41907378), and the Nanjing University Innovation and Creative Program for Ph.D. candidate (Grant No. CXCY19-60). We are grateful to the High Performance Computing Center (HPCC) of Nanjing University for doing the numerical calculations in this paper on its blade cluster system, and thank the MEIC team for providing the prior anthropogenic emissions (http://www.meicmodel.org/).

References

Appel, K. W., Pouliot, G. A., Simon, H., Sarwar, G., Pye, H. O. T., Napelenok, S. L., Akhtar, F., and Roselle, S. J.: Evaluation of dust and trace metal estimates from the Community Multiscale Air Quality (CMAQ) model version 5.0, Geoscientific Model Development, 6, 883-899, 10.5194/gmd-6-883-2013, 2013.

Alexe, M., Bergamaschi, P., Segers, A., Detmers, R., Butz, A., Hasekamp, O., Guerlet, S., Parker, R., Boesch, H., Frankenberg, C., Scheepmaker, R. A., Dlugokencky, E., Sweeney, C., Wofsy, S. C., and Kort, E. A.: Inverse modelling of CH4 emissions for 2010-2011 using different satellite retrieval products from GOSAT and SCIAMACHY, Atmospheric Chemistry and Physics, 15, 113-133, 2015.

Barbu, A. L., Segers, A. J., Schaap, M., Heemink, A. W., and Builtjes, P. J. H.: A multi-component data assimilation experiment directed to sulphur dioxide and sulphate over Europe, Atmospheric Environment, 43, 1622-1631, 2009.

Basu, S., Guerlet, S., Butz, A., Houweling, S., Hasekamp, O., Aben, I., Krummel, P., Steele, P., Langenfelds, R., Torn, M., Biraud, S., Stephens, B., Andrews, A., and Worthy, D.: Global CO2 fluxes estimated from GOSAT retrievals of total column CO2, Atmospheric Chemistry and Physics, 13, 8695-8717, 2013.

Bauwens, M., Compernolle, S., Stavrakou, T., Müller, J.-F., van Gent, J., Eskes, H., Levelt, P. F., van der A, R., Veefkind, J. P., Vlietinck, J., Yu, H., and Zehner, C.: Impact of Coronavirus Outbreak on NO2 Pollution Assessed Using TROPOMI and OMI Observations, 47, e2020GL087978, 10.1029/2020gl087978, 2020.

Bierman: Factorization methods for Discrete Sequential estimation, Academic Press, 1977.

Binkowski, F. S. and Roselle, S. J.: Models-3 community multiscale air quality (CMAQ) model aerosol component - 1. Model description, Journal of Geophysical Research-Atmospheres, 108, 10.1029/2001jd001409, 2003.

Brandhorst, N., Erdal, D., and Neuweiler, I.: Soil moisture prediction with the ensemble Kalman filter: Handling uncertainty of soil hydraulic parameters, Advances in Water Resources, 110, 360-370, 2017.

Bruhwiler, L. M. P., Michalak, A. M., Peters, W., Baker, D. F., and Tans, P.: An improved Kalman Smoother for atmospheric inversions, Atmos. Chem. Phys., 5, 2691-2702, 10.5194/acp-5-2691-2005, 2005.

Carlton, A. G., Turpin, B. J., Altieri, K. E., Seitzinger, S. P., Mathur, R., Roselle, S. J., and Weber, R. J.: CMAQ Model Performance Enhanced When In-Cloud Secondary Organic Aerosol is Included: Comparisons of Organic Carbon Predictions with Measurements, Environmental Science & Technology, 42, 8798-8802, 2008

Chen, D., Liu, Z., Ban, J., and Chen, M.: The 2015 and 2016 wintertime air pollution in China: SO2 emission changes derived from a WRF-Chem/EnKF coupled data assimilation system, Atmospheric Chemistry and Physics, 19, 8619-8650, 10.5194/acp-19-8619-2019, 2019.

Chen, D., Liu, Z., Fast, J., and Ban, J.: Simulations of sulfate-nitrate-ammonium (SNA) aerosols during the extreme haze events over northern China in October 2014, Atmospheric Chemistry and Physics, 16, 10707-10724, 10.5194/acp-16-10707-2016, 2016.

Chevallier, F., Bréon, F.-M., and Rayner, P. J.: Contribution of the Orbiting Carbon Observatory to the estimation of CO2 sources and sinks: Theoretical study in a variational data assimilation framework, 112, 10.1029/2006JD007375, 2007.

Clements, A. L., Fraser, M. P., Upadhyay, N., Herckes, P., Sundblom, M., Lantz, J., and Solomon, P. A.: Chemical characterization of coarse particulate matter in the Desert Southwest - Pinal County Arizona, USA, Atmospheric Pollution Research, 5, 52-61, 10.5094/apr.2014.007, 2014.

Clements, N., Hannigan, M. P., Miller, S. L., Peel, J. L., and Milford, J. B.: Comparisons of urban and rural PM10-2.5 and PM2.5 mass concentrations and semi-volatile fractions in northeastern Colorado, Atmospheric Chemistry and Physics, 16, 7469-7484, 10.5194/acp-16-7469-2016, 2016.

Daley, R.: Atmospheric Data Assimilation (gtSpecial IssueltData Assimilation in Meteology and Oceanography: Theory and Practice), Journal of the Meteorological Society of Japan. Ser. II, 75, 319-329, 1997.

Derber, J. C.: A VARIATIONAL CONTINUOUS ASSIMILATION TECHNIQUE, Monthly Weather Review, 117, 2437-2446, 1989.

de Foy, B., Lu, Z., Streets, D. G., Lamsal, L. N., and Duncan, B. N.: Estimates of power plant NOx emissions and lifetimes from OMI NO2 satellite retrievals, Atmospheric Environment, 116, 1-11, 10.1016/j.atmosenv.2015.05.056, 2015.

De Lannoy, G. J. M., Houser, P. R., Pauwels, V. R. N., and Verhoest, N. E. C.: State and bias estimation for soil moisture profiles by an ensemble Kalman filter: Effect of assimilation depth and frequency, 43, 2007.

Ding, J., van der A, R. J., Mijling, B., Levelt, P. F., and Hao, N.: NOx emission estimates during the 2014 Youth Olympic Games in Nanjing, Atmospheric Chemistry and Physics, 15, 9399-9412, 10.5194/acp-15-9399-2015, 2015.

Elbern, H., Strunk, A., Schmidt, H., and Talagrand, O.: Emission rate and chemical state estimation by 4-dimensional variational inversion, Atmospheric Chemistry and Physics, 7, 3749-3769, 10.5194/acp-7-3749-2007, 2007.

Evensen, G.: The Ensemble Kalman Filter for Combined State and Parameter Estimation MONTE CARLO TECHNIQUES FOR DATA ASSIMILATION IN LARGE SYSTEMS, Ieee Control Systems Magazine, 29, 83-104, 10.1109/mcs.2009.932223, 2009.

Feng, S., Jiang, F., Jiang, Z., Wang, H., Cai, Z., and Zhang, L.: Impact of 3DVAR assimilation of surface PM2.5 observations on PM2.5 forecasts over China during wintertime, Atmospheric Environment, 187, 34-49, 10.1016/j.atmosenv.2018.05.049, 2018.

Feng, S., Jiang, F., Wang, H., Shen, Y., Zheng, Y., Zhang, L., Lou, C., and Ju, W.: Anthropogenic emissions estimated using surface observations and their impacts on PM2.5 source apportionment over the Yangtze River Delta, China, Science of The Total Environment, 828, 154522, 2022

Feng, S., Jiang, F., Wu, Z., Wang, H., Ju, W., and Wang, H.: CO Emissions Inferred From Surface CO Observations Over China in December 2013 and 2017, Journal of Geophysical Research-Atmospheres, 125, 10.1029/2019jd031808, 2020a.

Feng, S., Jiang, F., Wang, H., Wang, H., Ju, W., Shen, Y., Zheng, Y., Wu, Z., and Ding, A.: NOx Emission Changes Over China During the COVID-19 Epidemic Inferred From Surface NO2 Observations, Geophysical Research Letters, 47, 10.1029/2020gl090080, 2020b.

Feng, S. and Jiang, F.: Anthropogenic air pollutant emissions over China inferred by Regional multi-

Air Pollutant Assimilation System (RAPAS v1.0), Zenodo, 10.5281/zenodo.4718290, 2021.

Gaspari, G. and Cohn, S. E.: Construction of correlation functions in two and three dimensions, Quarterly Journal of the Royal Meteorological Society, 125, 723-757, 10.1256/smsqj.55416, 1999.

Guenther, A. B., Jiang, X., Heald, C. L., Sakulyanontvittaya, T., Duhl, T., Emmons, L. K., and Wang, X.: The Model of Emissions of Gases and Aerosols from Nature version 2.1 (MEGAN2.1): an extended and updated framework for modeling biogenic emissions, Geoscientific Model Development, 5, 1471-1492, 10.5194/gmd-5-1471-2012, 2012.

Gurney, K. R., Law, R. M., Denning, A. S., Rayner, P. J., Pak, B. C., Baker, D., Bousquet, P., Bruhwiler, L., Chen, Y. H., Ciais, P., Fung, I. Y., Heimann, M., John, J., Maki, T., Maksyutov, S., Peylin, P., Prather, M., and Taguchi, S.: Transcom 3 inversion intercomparison: Model mean results for the estimation of seasonal carbon sources and sinks, Global Biogeochemical Cycles, 18, 10.1029/2003gb002111, 2004.

He, W., van der Velde, I. R., Andrews, A. E., Sweeney, C., Miller, J., Tans, P., van der Laan-Luijkx, I. T., Nehrkorn, T., Mountain, M., Ju, W., Peters, W., and Chen, H.: CTDAS-Lagrange v1.0: a high-resolution data assimilation system for regional carbon dioxide observations, Geoscientific Model Development, 11, 3515-3536, 10.5194/gmd-11-3515-2018, 2018.

Hinds, W.C.: Aerosol Technology: Properties, Behavior, and Measurement of Airborne Particles. New York: John Wiley, 1982.

Houtekamer, P. L. and Mitchell, H. L.: A sequential ensemble Kalman filter for atmospheric data assimilation, Monthly Weather Review, 129, 123-137, 10.1175/1520-0493(2001)129<0123:asekff>2.0.co;2, 2001.

Houtekamer, P. L. and Zhang, F.: Review of the Ensemble Kalman Filter for Atmospheric Data Assimilation, Monthly Weather Review, 144, 4489-4532, 10.1175/mwr-d-15-0440.1, 2016.

Inness, A., Blechschmidt, A. M., Bouarar, I., Chabrillat, S., Crepulja, M., Engelen, R. J., Eskes, H., Flemming, J., Gaudel, A., Hendrick, F., Huijnen, V., Jones, L., Kapsomenakis, J., Katragkou, E., Keppens, A., Langerock, B., de Maziere, M., Melas, D., Parrington, M., Peuch, V. H., Razinger, M., Richter, A., Schultz, M. G., Suttie, M., Thouret, V., Vrekoussis, M., Wagner, A., and Zerefos, C.: Data assimilation of satellite-retrieved ozone, carbon monoxide and nitrogen dioxide with ECMWF's Composition-IFS, Atmospheric Chemistry and Physics, 15, 5275-5303, 2015.

Jiang, F., Liu, Q., Huang, X., Wang, T., Zhuang, B., and Xie, M.: Regional modeling of secondary organic aerosol over China using WRF/Chem, Journal of Aerosol Science, 43, 57-73, 10.1016/j.jaerosci.2011.09.003, 2012a.

Jiang, F., Zhou, P., Liu, Q., Wang, T., Zhuang, B., and Wang, X.: Modeling tropospheric ozone formation over East China in springtime, Journal of Atmospheric Chemistry, 69, 303-319, 10.1007/s10874-012-9244-3, 2012b.

Jiang, F., Wang, H. M., Chen, J. M., Machida, T., Zhou, L. X., Ju, W. M., Matsueda, H., and Sawa, Y.: Carbon balance of China constrained by CONTRAIL aircraft CO2 measurements, Atmospheric Chemistry and Physics, 14, 10133-10144, 10.5194/acp-14-10133-2014, 2014.

Jiang, F., Wang, H., Chen, J. M., Ju, W., Tian, X., Feng, S., Li, G., Chen, Z., Zhang, S., Lu, X., Liu, J., Wang, H., Wang, J., He, W., and Wu, M.: Regional CO2 fluxes from 2010 to 2015 inferred from GOSAT XCO2 retrievals using a new version of the Global Carbon Assimilation System, Atmos. Chem. Phys., 21, 1963-1985, 10.5194/acp-21-1963-2021, 2021.

Jiang, W., Smyth, S., Giroux, E., Roth, H., and Yin, D.: Differences between CMAQ fine mode particle and PM2.5 concentrations and their impact on model performance evaluation in the lower Fraser valley, Atmospheric Environment, 40, 4973-4985, 10.1016/j.atmosenv.2005.10.069, 2006.

Jiang, Z., Jones, D. B. A., Worden, H. M., Deeter, M. N., Henze, D. K., Worden, J., Bowman, K. W., Brenninkmeijer, C. A. M., and Schuck, T. J.: Impact of model errors in convective transport on CO source estimates inferred from MOPITT CO retrievals, Journal Of Geophysical Research-Atmospheres, 118, 2073-2083, 2013a.

Jiang, Z., Liu, Z., Wang, T., Schwartz, C. S., Lin, H.-C., and Jiang, F.: Probing into the impact of 3DVAR assimilation of surface PM10 observations over China using process analysis, Journal of Geophysical Research: Atmospheres, 118, 6738-6749, 10.1002/jgrd.50495, 2013b.

Jiang, Z., Worden, J. R., Worden, H., Deeter, M., Jones, D. B. A., Arellano, A. F., and Henze, D. K.: A 15-year record of CO emissions constrained by MOPITT CO observations, Atmospheric Chemistry And Physics, 17, 4565-4583, 10.5194/acp-17-4565-2017, 2017.

Jin, J., Lin, H. X., Heemink, A., and Segers, A.: Spatially varying parameter estimation for dust emissions using reduced-tangent-linearization 4DVar, Atmospheric Environment, 187, 358-373, 10.1016/j.atmosenv.2018.05.060, 2018.

Kahnert, M.: Variational data analysis of aerosol species in a regional CTM: background error covariance constraint and aerosol optical observation operators, Tellus B, 60, 2008.

Kang, J.-S., Kalnay, E., Miyoshi, T., Liu, J., and Fung, I.: Estimation of surface carbon fluxes with an advanced data assimilation methodology, 117, 10.1029/2012JD018259, 2012.

Keppenne, C. L., Rienecker, M. M., Kurkowski, N. P., and Adamec, D. A.: Ensemble Kalman filter assimilation of temperature and altimeter data with bias correction and application to seasonal prediction, Nonlin. Processes Geophys., 12, 491-503, 2005.

Kleist, D. T., Parrish, D. F., Derber, J. C., Treadon, R., Wu, W.-S., and Lord, S.: Introduction of the GSI into the NCEP Global Data Assimilation System, Weather and Forecasting, 24, 1691-1705, 10.1175/2009waf2222201.1, 2009.

Kong, L., Tang, X., Zhu, J., Wang, Z., Pan, Y., Wu, H., Wu, L., Wu, Q., He, Y., Tian, S., Xie, Y., Liu, Z., Sui, W., Han, L., and Carmichael, G.: Improved Inversion of Monthly Ammonia Emissions in China Based on the Chinese Ammonia Monitoring Network and Ensemble Kalman Filter, Environmental Science & Technology, 53, 12529-12538, 10.1021/acsest.9b02701, 2019a.

Kong, L., Tang, X., Zhu, J., Wang, Z., Fu, J. S., Wang, X., Itahashi, S., Yamaji, K., Nagashima, T., Lee, H. J., Kim, C. H., Lin, C. Y., Chen, L., Zhang, M., Tao, Z., Li, J., Kajino, M., Liao, H., Sudo, K., Wang, Y., Pan, Y., Tang, G., Li, M., Wu, Q., Ge, B., and Carmichael, G. R.: Evaluation and uncertainty investigation of the NO2, CO and NH3 modeling over China under the framework of MICS-Asia III, Atmos. Chem. Phys. Discuss., 2019, 1-33, 10.5194/acp-2018-1158, 2019b.

Kurokawa, J.-i., Yumimoto, K., Uno, I., and Ohara, T.: Adjoint inverse modeling of NOx emissions over eastern China using satellite observations of NO2 vertical column densities, Atmospheric Environment, 43, 1878-1887, 10.1016/j.atmosenv.2008.12.030, 2009.

Laloyaux, P., Bonavita, M., Chrust, M., and Gürol, S.: Exploring the potential and limitations of weak-constraint 4D-Var, Quarterly Journal of the Royal Meteorological Society, 146, 4067-4082, 2020

Li, J.-d., Deng, Q.-h., Lu, C., and Huang, B.-l.: Chemical compositions and source apportionment

of atmospheric PM10 in suburban area of Changsha, China, Journal of Central South University of Technology, 17, 509-515, 2010.

Li, M., Zhang, Q., Kurokawa, J.-i., Woo, J.-H., He, K., Lu, Z., Ohara, T., Song, Y., Streets, D. G., Carmichael, G. R., Cheng, Y., Hong, C., Huo, H., Jiang, X., Kang, S., Liu, F., Su, H., and Zheng, B.: MIX: a mosaic Asian anthropogenic emission inventory under the international collaboration framework of the MICS-Asia and HTAP, Atmospheric Chemistry and Physics, 17, 935-963, 10.5194/acp-17-935-2017, 2017.

Liu, Z., Liu, Q., Lin, H.-C., Schwartz, C. S., Lee, Y.-H., and Wang, T.: Three-dimensional variational assimilation of MODIS aerosol optical depth: Implementation and application to a dust storm over East Asia, Journal of Geophysical Research: Atmospheres, 116, n/a-n/a, 10.1029/2011jd016159, 2011.

Lorenc, A. C.: Modelling of error covariances by 4D-Var data assimilation, Quarterly Journal of the Royal Meteorological Society, 129, 3167-3182, 2003.

Hamer, P. D., Bowman, K. W., Henze, D. K., Attie, J. L., and Marecal, V.: The impact of observing characteristics on the ability to predict ozone under varying polluted photochemical regimes, Atmospheric Chemistry and Physics, 15, 10645-10667, 2015.

Ma, C., Wang, T., Mizzi, A. P., Anderson, J. L., Zhuang, B., Xie, M., and Wu, R.: Multiconstituent Data Assimilation With WRF-Chem/DART: Potential for Adjusting Anthropogenic Emissions and Improving Air Quality Forecasts Over Eastern China, 124, 7393-7412, 10.1029/2019jd030421, 2019.

Meirink, J. F., Eskes, H. J., and Goede, A. P. H.: Sensitivity analysis of methane emissions derived from SCIAMACHY observations through inverse modelling, Atmospheric Chemistry and Physics, 6, 1275-1292, 10.5194/acp-6-1275-2006, 2006.

Maybeck: Stochastic Models, Estimation and Control Academic Press, 1979.

Miyazaki, K. and Eskes, H.: Constraints on surface NOx emissions by assimilating satellite observations of multiple species, Geophysical Research Letters, 40, 4745-4750, 10.1002/grl.50894, 2013.

Miyazaki, K., Eskes, H. J., and Sudo, K.: Global NOx emission estimates derived from an assimilation of OMI tropospheric NO2 columns, Atmospheric Chemistry and Physics, 12, 2263-2288, 10.5194/acp-12-2263-2012, 2012a.

Miyazaki, K., Eskes, H. J., Sudo, K., Takigawa, M., van Weele, M., and Boersma, K. F.: Simultaneous assimilation of satellite NO2, O-3, CO, and HNO3 data for the analysis of tropospheric chemical composition and emissions, Atmospheric Chemistry and Physics, 12, 9545-9579, 10.5194/acp-12-9545-2012, 2012b.

Miyazaki, K., Eskes, H., Sudo, K., Boersma, K. F., Bowman, K., and Kanaya, Y.: Decadal changes in global surface NOx emissions from multi-constituent satellite data assimilation, Atmospheric Chemistry and Physics, 17, 807-837, 2017.

Monteil, G., Houweling, S., Butz, A., Guerlet, S., Schepers, D., Hasekamp, O., Frankenberg, C., Scheepmaker, R., Aben, I., and Rockmann, T.: Comparison of CH4 inversions based on 15 months of GOSAT and SCIAMACHY observations, Journal of Geophysical Research-Atmospheres, 118, 11807-11823, 2013.

Nassar, R., Jones, D. B. A., Kulawik, S. S., Worden, J. R., Bowman, K. W., Andres, R.

J., Suntharalingam, P., Chen, J. M., Brenninkmeijer, C. A. M., Schuck, T. J., Conway, T. J., and Worthy, D. E.: Inverse modeling of CO2 sources and sinks using satellite observations of CO2 from TES and surface flask measurements, Atmospheric Chemistry and Physics, 11, 6029-6047, 2011.

Parrish, D. F. and Derber, J. C.: The National Meteorological Center's spectral statistical-interpolation analysis system, Monthly Weather Review, 120, 1747-1763, 10.1175/1520-0493(1992)120<1747:tnmcss>2.0.co;2, 1992.

Paulot, F., Jacob, D. J., Pinder, R. W., Bash, J. O., Travis, K., and Henze, D. K.: Ammonia emissions in the United States, European Union, and China derived by high-resolution inversion of ammonium wet deposition data: Interpretation with a new agricultural emissions inventory (MASAGE_NH3), Journal of Geophysical Research-Atmospheres, 119, 4343-4364, 2014.

Peng, Z., Liu, Z., Chen, D., and Ban, J.: Improving PM_{2. 5} forecast over China by the joint adjustment of initial conditions and source emissions with an ensemble Kalman filter, Atmospheric Chemistry and Physics, 17, 4837-4855, 10.5194/acp-17-4837-2017, 2017.

Peng, Z., Lei, L., Liu, Z., Su, J., Ding, A., Ban, J., Chen, D., Kou, X., and Chu, K.: The impact of multi-species surface chemical observation assimilation on air quality forecasts in China, Atmospheric Chemistry and Physics, 18, 10.5194/acp-18-17387-2018, 2018.

Peters, W., Jacobson, A. R., Sweeney, C., Andrews, A. E., Conway, T. J., Masarie, K., Miller, J. B., Bruhwiler, L. M. P., Petron, G., Hirsch, A. I., Worthy, D. E. J., van der Werf, G. R., Randerson, J. T., Wennberg, P. O., Krol, M. C., and Tans, P. P.: An atmospheric perspective on North American carbon dioxide exchange: CarbonTracker, Proceedings of the National Academy of Sciences of the United States of America, 104, 18925-18930, 10.1073/pnas.0708986104, 2007.

Peylin, P., Rayner, P. J., Bousquet, P., Carouge, C., Hourdin, F., Heinrich, P., Ciais, P., and contributors, A.: Daily CO2 flux estimates over Europe from continuous atmospheric measurements: 1, inverse methodology, Atmospheric Chemistry and Physics, 5, 3173-3186, 10.5194/acp-5-3173-2005, 2005.

Purser, R. J., Wu, W. S., Parrish, D. F., and Roberts, N. M.: Numerical aspects of the application of recursive filters to variational statistical analysis. Part I: Spatially homogeneous and isotropic Gaussian covariances, Monthly Weather Review, 131, 1524-1535, 10.1175//1520-0493(2003)131<1524:naotao>2.0.co;2, 2003.

Quan, J., Liu, Q., Li, X., Gao, Y., Jia, X., Sheng, J., Liu, Y., 2015. Effect of heterogeneous aqueous reactions on the secondary formation of inorganic aerosols during haze events. Atmospheric Environment 122, 306-312.

Rabier, F., McNally, A., Andersson, E., Courtier, P., Unden, P., Eyre, J., Hollingsworth, A., and Bouttier, F.: The ECMWF implementation of three-dimensional variational assimilation (3D-Var). II: Structure functions, Quarterly Journal Of the Royal Meteorological Society, 124, 1809-1829, 10.1256/smsqj.55002, 1998.

Reichle, R. H., McLaughlin, D. B., and Entekhabi, D.: Hydrologic data assimilation with the ensemble Kalman filter, Monthly Weather Review, 130, 103-114, 2002.

Richardson, H., Basu, S., and Holtslag, A. A. M.: Improving Stable Boundary-Layer Height Estimation Using a Stability-Dependent Critical Bulk Richardson Number,

Boundary-Layer Meteorology, 148, 93-109, 2013.

Ruiz, J. and Pulido, M.: Parameter Estimation Using Ensemble-Based Data Assimilation in the Presence of Model Error, Monthly Weather Review, 143, 1568-1582, 2015.

Sarwar, G., Simon, H., Bhave, P., and Yarwood, G.: Examining the impact of heterogeneous nitryl chloride production on air quality across the United States, Atmospheric Chemistry and Physics, 12, 6455-6473, 10.5194/acp-12-6455-2012, 2012.

Sasaki, Y.: SOME BASIC FORMALISMS IN NUMERICAL VARIATIONAL ANALYSIS, Monthly Weather Review, 98, 875-&, 1970.

Schneising, O., Buchwitz, M., Burrows, J. P., Bovensmann, H., Bergamaschi, P., and Peters, W.: Three years of greenhouse gas column-averaged dry air mole fractions retrieved from satellite - Part 2: Methane, Atmospheric Chemistry and Physics, 9, 443-465, 2009.

Schwartz, C. S., Liu, Z., Lin, H.-C., and Cetola, J. D.: Assimilating aerosol observations with a "hybrid" variational-ensemble data assimilation system, Journal Of Geophysical Research-Atmospheres, 119, 4043-4069, 10.1002/2013jd020937, 2014.

Sekiyama, T. T., Tanaka, T. Y., Shimizu, A., and Miyoshi, T.: Data assimilation of CALIPSO aerosol observations, Atmospheric Chemistry and Physics, 10, 39-49, 10.5194/acp-10-39-2010, 2010.

Shen, Y., Jiang, F., Feng, S., Zheng, Y., Cai, Z., and Lyu, X.: Impact of weather and emission changes on NO2 concentrations in China during 2014–2019, Environmental Pollution, 269, 116163, 10.1016/j.envpol.2020.116163, 2021.

Shi, X. and Brasseur, G. P.: The Response in Air Quality to the Reduction of Chinese Economic Activities During the COVID-19 Outbreak, 47, e2020GL088070, 10.1029/2020gl088070, 2020.

Stanevich, I., Jones, D. B. A., Strong, K., Keller, M., Henze, D. K., Parker, R. J., Boesch, H., Wunch, D., Notholt, J., Petri, C., Warneke, T., Sussmann, R., Schneider, M., Hase, F., Kivi, R., Deutscher, N. M., Velazco, V. A., Walker, K. A., and Deng, F.: Characterizing model errors in chemical transport modeling of methane: using GOSAT XCH4 data with weak-constraint four-dimensional variational data assimilation, Atmospheric Chemistry and Physics, 21, 9545-9572, 2021.

Stavrakou, T., Müller, J.-F., Boersma, K. F., De Smedt, I., and van der A, R. J.: Assessing the distribution and growth rates of NOx emission sources by inverting a 10-year record of NO2 satellite columns, 35, 10.1029/2008gl033521, 2008.

Sun, A. Y., Morris, A., and Mohanty, S.: Comparison of deterministic ensemble Kalman filters for assimilating hydrogeological data, Advances in Water Resources, 32, 280-292, 10.1016/j.advwatres.2008.11.006, 2009.

Takagi, H., Saeki, T., Oda, T., Saito, M., Valsala, V., Belikov, D., Saito, R., Yoshida, Y., Morino, I., Uchino, O., Andres, R. J., Yokota, T., and Maksyutov, S.: On the Benefit of GOSAT Observations to the Estimation of Regional CO₂ Fluxes, SOLA, 7, 161-164, 10.2151/sola.2011-041, 2011.

Tang, X., Zhu, J., Wang, Z. F., and Gbaguidi, A.: Improvement of ozone forecast over Beijing based on ensemble Kalman filter with simultaneous adjustment of initial conditions and emissions, Atmospheric Chemistry And Physics, 11, 12901-12916, 10.5194/acp-11-12901-2011, 2011.

Tang, X., Zhu, J., Wang, Z. F., Wang, M., Gbaguidi, A., Li, J., Shao, M., Tang, G. Q., and Ji, D. S.:

Inversion of CO emissions over Beijing and its surrounding areas with ensemble Kalman filter, Atmospheric Environment, 81, 676-686, 10.1016/j.atmosenv.2013.08.051, 2013.

Wang, C., Lei, L., Tan, Z.-M., and Chu, K.: Adaptive Localization for Tropical Cyclones With Satellite Radiances in an Ensemble Kalman Filter, Frontiers in Earth Science, 8, 10.3389/feart.2020.00039, 2020.

Wang, H., Jiang, F., Wang, J., Ju, W., and Chen, J. M.: Terrestrial ecosystem carbon flux estimated using GOSAT and OCO-2 XCO2 retrievals, Atmospheric Chemistry and Physics, 19, 12067-12082, 2019a.

Wang, N., Lyu, X., Deng, X., Huang, X., Jiang, F., and Ding, A.: Aggravating O3 pollution due to NOx emission control in eastern China, Science of The Total Environment, 677, 732-744, 2019b.

Wang, Y. H., Hu, B., Ji, D. S., Liu, Z. R., Tang, G. Q., Xin, J. Y., Zhang, H. X., Song, T., Wang, L. L., Gao, W. K., Wang, X. K., and Wang, Y. S.: Ozone weekend effects in the Beijing-Tianjin-Hebei metropolitan area, China, Atmospheric Chemistry and Physics, 14, 2419-2429, 2014.

Wang, Z., Li, Y., Dong, X., Sun, R., Sun, N., and Pan, L.: Analysis on weekend effect of air pollutants in urban atmosphere of Beijing, Journal of University of Chinese Academy of Sciences, 32, 843-850, 2015.

Wang, Z., Wang, W., Tham, Y.J., Li, Q., Wang, H., Wen, L., Wang, X., Wang, T., 2017. Fast heterogeneous N2O5 uptake and ClNO2 production in power plant and industrial plumes observed in the nocturnal residual layer over the North China Plain. Atmospheric Chemistry and Physics 17, 12361-12378.

Wecht, K. J., Jacob, D. J., Sulprizio, M. P., Santoni, G. W., Wofsy, S. C., Parker, R., Boesch, H., and Worden, J.: Spatially resolving methane emissions in California: constraints from the CalNex aircraft campaign and from present (GOSAT, TES) and future (TROPOMI, geostationary) satellite observations, Atmospheric Chemistry and Physics, 14, 8173-8184, 2014.

Wu, H., Tang, X., Wang, Z., Wu, L., Li, J., Wang, W., Yang, W., and Zhu, J.: High-spatiotemporal-resolution inverse estimation of CO and NOx emission reductions during emission control periods with a modified ensemble Kalman filter, Atmospheric Environment, 236, 10.1016/j.atmosenv.2020.117631, 2020.

Wu, W. S., Purser, R. J., and Parrish, D. F.: Three-dimensional variational analysis with spatially inhomogeneous covariances, Monthly Weather Review, 130, 2905-2916, 10.1175/1520-0493(2002)130<2905:tdvaws>2.0.co;2, 2002.

Yang, W., Li, J., Wang, W., Li, J., Ge, M., Sun, Y., Chen, X., Ge, B., Tong, S., Wang, Q., and Wang, Z.: Investigating secondary organic aerosol formation pathways in China during 2014, Atmospheric Environment, 213, 133-147, 2019.

Zhang, F., Weng, Y., Sippel, J. A., Meng, Z., and Bishop, C. H.: Cloud-Resolving Hurricane Initialization and Prediction through Assimilation of Doppler Radar Observations with an Ensemble Kalman Filter, Monthly Weather Review, 137, 2105-2125, 10.1175/2009mwr2645.1, 2009a.

Zhang, L., Chen, Y., Zhao, Y., Henze, D. K., Zhu, L., Song, Y., Paulot, F., Liu, X., Pan, Y., Lin, Y., and Huang, B.: Agricultural ammonia emissions in China: reconciling bottom-up and top-down estimates, Atmospheric Chemistry and Physics, 18, 339-355, 2018.

Zhang, Q., Streets, D. G., Carmichael, G. R., He, K. B., Huo, H., Kannari, A., Klimont, Z., Park, I.

S., Reddy, S., Fu, J. S., Chen, D., Duan, L., Lei, Y., Wang, L. T., and Yao, Z. L.: Asian emissions in 2006 for the NASA INTEX-B mission, Atmospheric Chemistry and Physics, 9, 5131-5153, 10.5194/acp-9-5131-2009, 2009b.

Zhang, S., Zheng, X., Chen, J. M., Chen, Z., Dan, B., Yi, X., Wang, L., and Wu, G.: A global carbon assimilation system using a modified ensemble Kalman filter, Geosci. Model Dev., 8, 805-816, 10.5194/gmd-8-805-2015, 2015.

Zhang, X., Liu, J., Han, H., Zhang, Y., Jiang, Z., Wang, H., Meng, L., Li, Y. C., and Liu, Y.: Satellite-Observed Variations and Trends in Carbon Monoxide over Asia and Their Sensitivities to Biomass Burning, Remote Sensing, 12, 10.3390/rs12050830, 2020.

Zheng, B., Tong, D., Li, M., Liu, F., Hong, C., Geng, G., Li, H., Li, X., Peng, L., Qi, J., Yan, L., Zhang, Y., Zhao, H., Zheng, Y., He, K., and Zhang, Q.: Trends in China's anthropogenic emissions since 2010 as the consequence of clean air actions, Atmospheric Chemistry And Physics, 18, 14095-14111, 10.5194/acp-18-14095-2018, 2018.